New shapemeter roll technology based on Fiber Bragg Grating technology for on-line flatness monitoring of thin cold rolled metal sheets

Sylvain Magne, Nicolas Legrand, Stéphane Ertz, Gwenael Jouvin, Vivien André, Guillaume Laffont, Laurent Boissonnet

New shapemeter roll technology based on Fiber Bragg Grating technology for on-line flatness monitoring of thin cold rolled metal sheets

S. Magne,[1,a, b)] N. Legrand,[2)] S. Ertz,[2,c)] G. Jouvin,[1)] V. André,[2,c)] G. Laffont,[1)] and L. Boissonnet,[3)]

[1]*Université Paris-Saclay, CEA, List, F-91120, Palaiseau, France*

[2]Arcelor-Mittal Chicago USA, R&D, 3001 East Columbus Drive, East Chicago, IN 46312, USA

[3]*C-TEC Constellium Technology, Centr'Alp, 725 rue Aristide Bergès CS10027, F-38341 Voreppe, France*

The shape of laminated products is a crucial parameter in high-speed and high-volume finishing lines where they must fulfill tight tolerances. Latent defects are detected by flatness rolls (or shapemeter rolls) inserted in the manufacturing line for online flatness control. A prototype of flatness roll has been developed with high spatial resolution (5 mm) and measurement capability over a thickness range of [0.1-1] mm to evaluate flatness and residual stresses of flat metal strip products manufactured by continuous cold rolling (ultra-thin sheets for packaging and automotive markets). The flatness roll prototype relies on pressure-induced strain sensing on segmented blades using Fiber Bragg Grating (FBG) technology. Synchronous measurement of the flatness profile across strip width rejects disturbances of strip tension during rolling. We provide a proof-of-concept on pilot lines in both static and dynamic conditions (*e.g.* roll in rotation and in contact with a strip under tension) and the sensing mechanism shows a capability above 3. This combination of performances remains unique up to now. Inter-blade crosstalk appears to be an important issue. We propose a crosstalk model that agrees with experimental coupling coefficients. A crosstalk matrix inversion yields the distribution in contact pressure from strain data measured on reverse side. Additional work will be required to use the flatness roll in industrial conditions.

I. INTRODUCTION

Since 1967 and the first flatness roll commercialized by the ABB Co. (Asea Brown Boveri), many commercial rolls were proposed on the market, involving several proprietary sensing mechanisms based on direct pressure sensing (pressductor, piezoelectric gauges), pressure-to-strain conversion (electrical strain gauges) or pressure-to-displacement conversion (Linear-Variable Displacement Transducer (LVDT)). However, the online flatness control of thin (< 0.5 mm) cold laminated metallic strips is still challenging because it requires a highly sensitive (kPa) and spatially accurate (mm) embedded pressure monitoring system. Flatness sensors are classified according to whether they rely on contact or non-contact methods [1-3].

[a)] CEA List, DM2I/SCI/LCFO, PC72, Bt 516, CEA Saclay, 91191 Gif-sur-Yvette, France,

[b)] Author to whom correspondence should be addressed. Electronic mail: sylvain.magne@cea.fr.

[c)] Arcelor-Mittal Global R&D, voie romaine, BP 30320, F57283 Maizières-les-Metz, France

Non-contact flatness sensors are based on optical (laser scanning optical triangulation, fringe projection, diffused light), electromagnetic or capacitive measurements. These solutions deliver shape-related signals, indicative of manifest defects, and usually operate at low sheet tension. However, optical methods might not operate properly with surface-contaminated or highly reflective products.

Contact sensors are flatness rolls inserted in the manufacturing line. In this configuration, the strip is bent along the roll surface and the resulting pressure distribution is monitored by pressure sensors disposed along the roll axis. The distribution in tensile strength is then retrieved from the pressure pattern and its deviation (with respect to an average value) is used as input vector for the Automatic Flatness Control (AFC) system, see Fig. 1 [1-3].

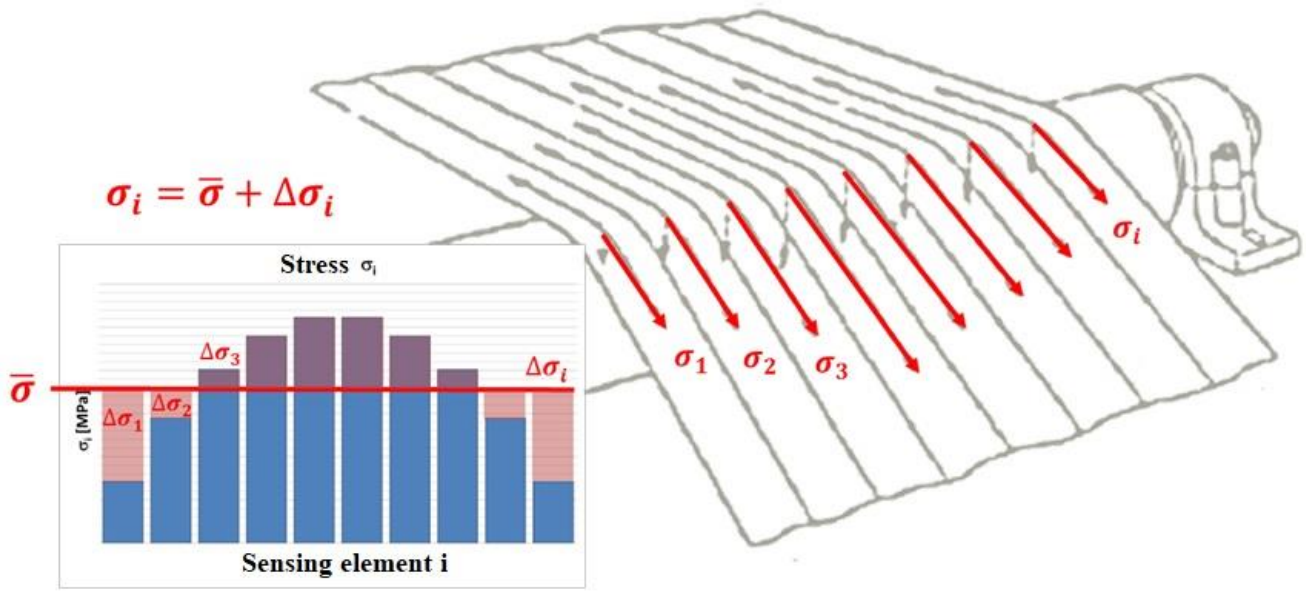

FIG. 1. Typical stress distribution measured along a strip by a flatness roll. The input vector for AFC is the stress deviation with respect to the average value (the strip is virtually segmented for sake of clarity), from [2].

Contact sensors therefore measure latent defects, *i.e.* defects that are not immediately visible but will appear once tension is released. Furthermore, they are used for the inspection of thin strips (< 1 mm) because bending-induced plastic deformation prevents from inspecting thicker products. The force F applied by the strip onto the roll surface depends both on traction force T and wrap angle α [2]:

$$F = 2 \cdot T \cdot \sin(\alpha/2)\,, \tag{1}$$

Let us consider the tensile stress τ (strip tension) applied to the strip as:

$$\tau = {}^{T}/_{(W \cdot t)}\,, \tag{2}$$

where W and t are the strip width and thickness respectively. Since the covered surface is αRW (where R is the radius of the roll), the average contact pressure P applied by the strip onto the roll surface writes as follows:

$$P = 2 \cdot \tau \cdot ({}^{t}/_{R}) \cdot \sin(\alpha/2)/\alpha\,, \tag{3}$$

The average contact pressure is proportional to strip thickness and tension (usually of several tens of MPa for steel strips). Moreover, it does not significantly change with wrap angle because both force and contact surface are proportional to it. The wrap angle must be large enough to cover the sensing surface onto the roll. As far as thin strips (0.1 mm to 0.2 mm) are concerned, the contact pressure may be considered as constant around the circumference of the contact surface. In practice however, the distribution in contact pressure usually follows a figure-of-M shape, particularly for thick strips. The contact pressure at mid-part is often underestimated when applying Eq. (3) because it is usually higher at both entrance and exit parts of the contact, out of the sensing surface.

The strip is usually considered as the superposition of parallel elementary strips (of width equal to the spatial resolution of the roll, see Fig. 1). Rolling engineers customarily take as reference a differential strain value of 50 microstrains between adjacent elementary strips in order to estimate the performance in flatness detection [1]. The rolling industry is accustomed to using the I-unit index notation (1 I = 10 microstrains = 10^{-5}). The differential strip tension between parallel elementary strips that corresponds to 5 I (50 microstrains) is then:

$$\Delta\tau = 5 \cdot 10^{-5} \cdot E', \tag{4}$$

where E' is the apparent Young modulus of the material (~ 210 GPa for steel and ~ 79 GPa for aluminum). The 5-I differential strip tension Δτ is then 10.5 MPa for steel and 3.95 MPa for aluminum. It is worthwhile noticing that these values only depend on strip material.

Flatness rolls necessitate a minimum strip tension to operate properly (typically several tens of MPa). From Eq. (3), the ratio P/τ is about 10^{-3} for a 300-mm diameter roll and a 0.2-mm thick strip. The consequence of this is that the differential contact pressure ΔP is three orders of magnitude lower than the differential strip tension Δτ, i.e. about 10 kPa and 5 kPa for 0.2-mm and 0.1-mm thick steel strips respectively (granted that the 5-I differential strip tension is 10 MPa for steel).

Finally, rolling engineers evaluate the metrological performance of a flatness roll by use of a dimensionless factor called capability, written as:

$$C = 0.25 \cdot {}^{\sigma_f}/_{\sigma_s}\,, \tag{5}$$

where σ_f and σ_s are the requested flatness uncertainty and the measurement uncertainty of the sensor (at 1-σ) respectively. The C-coefficient must be higher than unity in order to comply with industrial use. Practically, it means that the uncertainty in pressure sensing (at kHz rate) must be less than ¼th the 5-I flatness uncertainty, i.e. less than 1.25 kPa for 0.1-mm thick steel strips. This illustrates the need for a high bandpass highly sensitive pressure sensor for monitoring thin strip flatness.

In the following, we start from a review of the state-of-the-art of current flatness roll technologies and their limitations and we get into the details of the conception of the flatness roll prototype.

II. STATE-OF-THE-ART OF FLATNESS ROLL TECHNOLOGIES

Most contact shapemeters are rotating rolls inserted into the manufacturing line. Roll dimensions are typically 160 mm up to 700 mm in diameter and may be 2.4 m wide. Most rolls may operate at linear speeds up to 4000 m/min (i.e. 66 rd/s for a 30-cm roll). They are often equipped with four sensing lines (sometimes six) placed along their circumference, thus providing four recordings per turn (the number of sensing lines is always a multiple of two in order to balance inertia forces). According to this design, the sensing zone only covers several percents of the perimeter (duty factor ~ several %) and practically, encoders are used to trigger data acquisition with angular orientation. At such speed, the acquisition data rate should be at least of several kHz, in proportion inversely related to the duty factor.

Finally, the periodicity of the pressure signal provides an elegant way to discriminate in the time domain pressure or strain signals *vs* temperature effects. The difference between on-contact and off-contact signals is proportional to contact pressure thereby eliminating temperature influence granted that pressure or strain signals change much more rapidly than temperature (the reference strain (off contact)) is recorded several tens of milliseconds earlier than the pressure-induced strain (in contact)).

Such devices are reliable, fatigue-resistant and guaranteed for a minimum lifetime of 20 years. The uncertainty in pressure (or force) measurement is typically 0.1 % full scale (FS). Conditioning electronics are often located onto the stator, protected by a flanged housing. Non-contact rotor-to-stator data transmission devices are preferred to rotating joints due to lack of lateral space and because of the short Mean-Time-Between Failure (MTBF) of these devices. Rolls are also watertight to prevent water or oil ingress.

In the following, commercial flatness rolls are categorized according to whether they provide direct pressure monitoring or pressure-induced displacement (or strain) monitoring. Every manufacturer (ABB, BFI, VAI-Clecim, etc.) has developed its proprietary pressure sensing technology [2].

A. Flatness rolls equipped with pressure sensing technology

Most rolls based on pressure (or force) monitoring incorporate rigid sensors (the sleeve transmits the force/pressure to the sensors and is not deformed).

The Swiss-Swedish company ABB implemented in 1967 the first flatness roll equipped with the so-called Pressductor Technology, based on a magneto-elastic transducer involving a solenoid pair. A first solenoid generates a magnetic field and

the amount of magnetic flux coupled to a second (receiver) solenoid is modified according to applied load, thereby changing the voltage.

ABB proposes three kinds of rolls: I/ standard roll, II/ foil roil for low-tension applications and III/ seamless roll for high strip surface quality finishing (i.e. bright-annealed stainless steel). The two first rolls involve shrink-on rings with the aim to minimize pressure crosstalk between adjacent Pressductors (ABB claims for a typical crosstalk of 25 %). Two sensor widths are available: 26 mm and 52 mm.

The German research institute BFI (VDEh Betriebsforschungsinstitut) developed another flatness roll equipped with piezoelectric pressure gauges (9051 A, Kistler Company). Compared to Pressductors, piezoelectric sensors do not need local power supply, therefore simplifying their use. Furthermore, they show very high stiffness (9 kN/µm) and pressure sensitivity. Each roll is made of a continuous (seamless) cylinder with drilled bores parallel to roll axis, accommodating cylinders that hosts prestressed sensors. The spatial resolution is 25 mm (strip edge area) or 50 mm (strip center area). The thickness of the sleeve (i.e. roll surface-to-sensor distance) is 10-12 mm for steel rolling and 6 mm for aluminum rolling. BFI licensed this technology to several companies (Achenbach Buschhütten GmbH, SMS DEMAG AG, Siemens AG, Friedrich Vollmer Feinmessgerätebau GmbH, Sundwig, Kobe Steel Ltd., etc.), making it a standard flatness roll device.

Finally, another flatness roll was recently proposed by the Czech company UVB-Technik. It involves 16 separate rings, each one rolling over two support bearings. The force applied by the strip transmits onto both bearings through load sensors. Each ring is 33-mm wide. This last conception conveys several advantages: I/ the recording electronics is located outside the rotating roll (thus avoiding rotary joint so simplifying signal transfer), II/ a pressure measurement is possible even if the roll does not turn and III/ the duty factor is unity. However, unlike rotating rolls, this new concept requires a dedicated temperature *vs* pressure discrimination method since the gauges are static. Furthermore, the manufacturer does not give the crosstalk figure between adjacent rings.

B. Flatness rolls equipped with displacement/strain sensing technology

Another class of flatness rolls involves pressure-induced displacement (or strain) monitoring rather than pure pressure monitoring. For example, Planicim VAI-Clecim (VOEST-ALPINE Industrieanlagenbau GmbH, acquired by Siemens Co.) designed a seamless flatness roll equipped with LVDTs, as illustrated in Fig. 2 [4].

Contact pressure is inferred from displacement measurement by use of a calibration law taking into account elasticity relationships. Since the sensing mechanism is based on a displacement measurement, the sleeve of the Planicim roll is made thinner (1.5 mm), i.e. more flexible than those designed for direct pressure sensing. However, the spatial resolution is 60 mm, limited by the size of the LVDTs. The capability is estimated at 2 for 5-I defects.

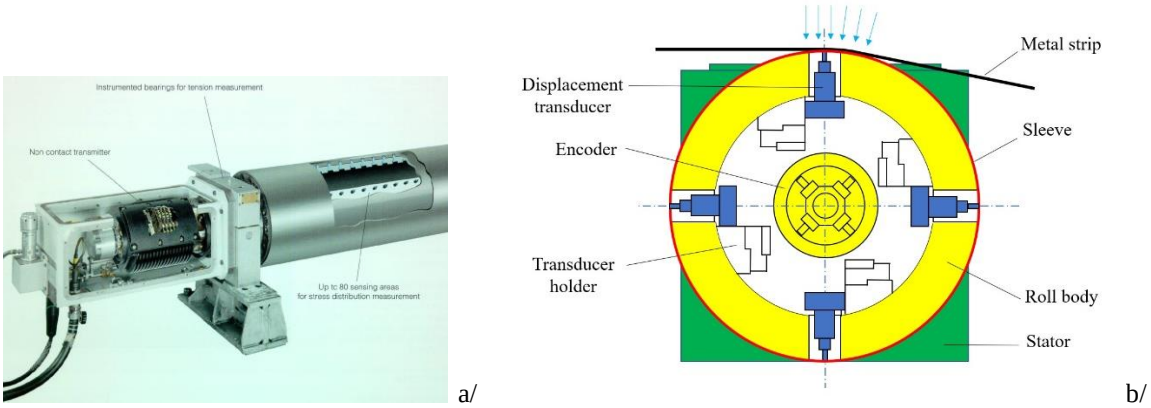

a/ b/

FIG. 2. Example of commercial flatness roll based on LVDT displacement sensing technology (Planicim, VAI-Clecim (now Siemens)). a/ view of the roll, b/ Simplified sketch of roll section showing 4 LVDTs placed at 90° each in order to provide 4 recordings per turn (adapted from commercial documentation from VAI-Clecim, encoder contact not shown).

This short review shows that the upmost limitation of above existing roll technologies is sensor size (typically 25 mm). Current roll technologies are limited in spatial resolution, not amenable to thin strip monitoring that requires a sub-cm resolution. High stress gradients at edges of thin strips are merely not detected using commercial roll technologies, with potential risk of strip break.

A second limitation is pressure data synchronicity along the roll length. The pressure readout must be performed simultaneously over the strip contact. It therefore precludes sensor offsetting in order to reduce the interspace between them, in the hope of artificially improving localization. Indeed, by doing so, the sensors are no longer aligned over a straight line (no longer parallel to the roll axis) so that they provide pressure data that are no more synchronized and spoiled by undesirable mechanical effects (roll unbalance or eccentricity of the winding machine).

A real-time data acquisition must be performed as well, over each sensing line, at a minimal data rate of 10 kHz in order to cope with linear speeds of industrial plant lines (up to 4000 m/min).

Finally, existing sensing technologies are not prone to multiplexing. A large amount of wires and connections spread out inside the roll, with associated complexity in deployment, connection, and data transfer. The number of sensors involved into a

commercial roll is width-dependent and is typically of several hundreds. It is doomed to increase as spatial resolution gets smaller, therefore raising additional multiplexing, deployment and cost issues that hamper a future increase in capacity. As an example, let us consider a 2-m wide roll equipped with four sensing lines, each one being composed of eighty 5-mm large sensors (at both edges) and sixty 20-mm large sensors (at center), the number of sensors for an entire roll would then be: $4\ lines \cdot (60 + 2 \cdot 80) = 880$.

The objective of the present work is to investigate an innovative flatness roll design of improved spatial accuracy, pressure sensitivity, data synchronicity and multiplexing capability in order to overcome issues encountered with conventional rolls for flatness control of thin laminated strips obtained by cold rolling. The flatness roll prototype relies on pressure-induced strain sensing on segmented blades using Fiber Bragg Grating (FBG) technology. To the best of our knowledge, this is a world-first achievement.

Fiber Bragg sensing technology holds great promise for improving performance in flatness roll technology dedicated to cold rolling. FBG sensors provide similar metrological performance to conventional devices (piezoelectric, strain gauges, etc.) but convey additional benefits such as lightweight, small size, high-frequency data recording. Wavelength-Division-Multiplexing (WDM) contributes to simplify both deployment and connection issues inside the roll structure as well because several FBGs are addressable along a single fiber. Finally, electromagnetic (EM) immunity of FBG sensors is an added benefit, granted that the FBG readout unit associated with the roll is EM-compliant (i.e. protected in an EMC enclosure).

C. Overcoming current issues with FBG sensing technology

Fiber Bragg sensing technology is a smart solution aiming at solving above-mentioned issues. Fiber Bragg Gratings (FBG) are tiny transducers, multiplexed in the spectral domain (Wavelength-Division Multiplexing - WDM) along a single fiber strand thus providing wavelength-encoded position and simplifying both deployment and connection procedures.

The description of FBG photo-inscription techniques and Bragg detection algorithms is out of scope of this paper. The reader is referred to review papers and books [5-7].

FBGs are simultaneously sensitive to axial strain, pressure and temperature. Sensitivities for a bare fiber are respectively: 1.21 pm/µstrain, -3.5 pm/MPa, about 10-12 pm/K depending on fiber composition. As most readout units exhibit spectral resolutions of the order of the picometer (pm), one can see that usual metrological resolutions for bare fibers are of the order of 1 µstrain, 0.1 K and 0.3 MPa (3 bar) respectively.

The pressure sensitivity of FBGs may be enhanced by applying a thick polymer coating onto it. Gains in pressure sensitivity of up to 20 have been demonstrated, thus lowering the pressure resolution down to 0.015 MPa (15 kPa) [8]. Based on this principle, researchers from IPHT (Jena, Germany) investigated the use of FBGs (Draw-Tower Gratings (DTG®), provided by the FBGS company) as load/pressure gauges embedded into the polymer coating of a roll for a paper machine, in collaboration with the Voith Company [9]. The FBGs monitored the pressure along the contact (nip) between two adjacent rolls, taking profit of the gain in pressure sensitivity provided by the polymer. A compact and robust proprietary FBG readout unit (called NIP vision™) was embedded into the roll, powered by an autonomous power supply, and the data were transmitted through a wireless link. IPHT claims their readout unit can withstand accelerations up to 300 g because of its compactness (low inertial forces). The readout device is a polychromator equipped with a concave diffraction grating and the optical source is a SuperLuminescent Diode (SLED) providing a broadband emission in the range [800 nm - 860 nm] allowing for multiplexing up to 32 sensors along a single fiber strand. The choice of a SLED was motivated by the use of a cheap mass-produced Si-based CCD line detector for the recording of the Bragg spectra as an alternative to usual InGaAs detectors used in the third telecommunication window (1.55 µm).

IPHT claims for continuous measurement along the roll profile, thanks to the WDM capability of the FBGs. Unfortunately, Ref. [9] does not provide enough data to assess for the global performances of the NIP Vision system (pressure sensitivity, range, resolution, repeatability, etc.).

Commercial FBG readout units actually compete with previously described conventional sensing mechanisms in terms of sensing range and strain resolution (i.e. 0.1 % FS). A dynamic range large enough (at least 3 orders of magnitude) is seeked for the contact pressure data in order to guarantee a minimum Signal-to-Noise Ratio (SNR) to the flatness vector (differential vector) that will be delivered to the AFC system. In this respect, bare or polymer-coated FBGs are not appropriate to low-pressure (kPa) detection because their pressure sensitivity is too low. Moreover, the use of thick polymer coatings are likely to induce calibration drift in time due to aging and creep issues.

III. DESCRIPTION OF THE FBG-BASED FLATNESS ROLL PROTOTYPE

FBGs are sensitive strain gauges exhibiting high directivity (i.e. FBGs are mostly sensitive to the strain component oriented towards fiber axis). As such, the flatness roll prototype involves pressure-induced strain monitoring and belongs to the second category, similarly to the Planicim roll.

A. Design of the flatness roll

The prototype roll is 300-mm wide and its external diameter is 296 mm. The approach used was to hollow the roll material out below the surface to create a cylinder void. Two cylinders (∅ = 54.5 mm) were initially drilled at 180° from each other (for sake of inertia balance). By doing so, the thickness of the shell is not constant within the roll section (as shown in Fig. 3a) as it results from the intersection of a small eccentric cylinder hole inside a greater cylinder. The thinnest part was 2-mm thick.

FBGs are then bonded onto the internal part of the shell, used as proof-body in order to measure the pressure-induced strain in the pressure range [kPa - MPa]. We adjusted shell material and size so that the pressure-induced strain remains lower than the maximum elastic limit within the pressure range of interest. In this work, E335 steel was used for manufacturing the prototype roll. This high-performance (non-alloy) carbon steel is often used for mechanical engineering. Its Young modulus is 190 GPa and its Poisson coefficient is 0.29. Its elastic limit is 335 MPa that corresponds to a maximum elastic strain of 1760 microstrain.

The limit of detection (LOD) in strain is twice the spectral resolution of the FBG readout unit (~ ± 0.3 pm, see III.C) granted that the Bragg shift is obtained by subtracting Bragg wavelengths when the strip is on and off contact respectively. The upper limit of strain range is the elastic domain of E335 steel (~ 1760 μstrain or 2130 pm) although in practice a conservative value is considered (typ. 1000 microstrains) to avoid hysteresis effects due to plasticity. Therefore, the LOD is less than 0.1 % FS, in accordance with specifications and alike conventional roll technologies. The linear strain (pressure) range is typically three orders of magnitude.

A first conception (cylinder hole-in-cylinder, Fig. 3a) was modeled using Finite-Element (FE) Modeling (Abaqus, Dassault Systemes, France). Radial (ε_{rr}), orthoradial ($\varepsilon_{\theta\theta}$) and longitudinal ($\varepsilon_z$) strain components along the internal surface were calculated as a function of local or distributed force applied on top of the shell (z is the axis of the cylinder hole, θ is the angle with respect to hole center). The strain data were calculated as a function of θ (vertical axis is taken at 0°). This preliminary work revealed that the orthoradial pressure-to-strain sensitivity is strongly angle-dependent, as confirmed by analytical calculations of stresses along the surface of an eccentric circular hole under radial forces performed in bipolar coordinates [10-

11]. In the case of a uniformly distributed force (representative of a strip contact), FE modeling showed that $e_{\vartheta\vartheta}$ and err are of opposite sign and both reach a maximum value for a critical angle of 24.5°. Furthermore, the orthoradial strain ($e_{\vartheta\vartheta}$) is about three times larger than the radial strain (err), usually monitored by other rolls (e.g. Planicim).

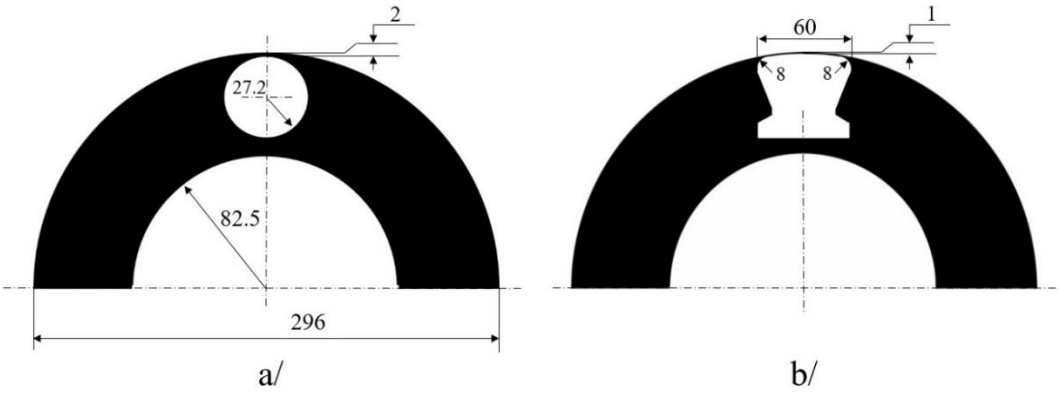

FIG. 3. Hole conceptions modeled and experimentally tested for pressure-to-strain monitoring purpose.
a/ Cylinder hole-in-cylinder, b/ Escutcheon in-cylinder.

We tested this first conception (Fig. 3a) by bonding several FBGs along an orthoradial configuration (i.e. we bonded the fiber along a circular section inside the shell). A load was uniformly applied on top of the shell using an applicator (60-mm large, 50-mm long, radius = 300 mm) connected in series with a load sensor (Wagezelle U1). Each grating were 2-mm long so covering an angle of about 5°.

The strain-to-load sensitivity was ~ -0.9 pm/kg in the angular sector 20-25°. Translated into pressure units, the maximum pressure-to-strain sensitivity was -0.027 pm/kPa. Given the resolution in Bragg measurements (~ ± 0.6 pm), it means that this first conception leads to a LOD in pressure of about 23 kPa which was too high regarding specifications.

We decided to implement a second conception (shown on Fig. 3b) with the aim to reduce shell stiffness and to improve the pressure-to-strain figure. It involves an escutcheon-shaped space under the roll surface (Fig. 4a and 4b). Another machining was then performed that left a thinned shell over a distance of 44 mm. This portion of shell is connected to the roll body by cylinder-shaped clamps that end up to vertical edges (edge-to-edge distance is 60 mm). As the fiber is wound inside the clamp part, we chose a radius of curvature of 8 mm to minimize bending-induced strain on the fiber and eliminate the risk of fiber break (most telecommunication fibers may withstand smaller radius of curvature (typically down to 5 mm)). The other important consequence of this large radius within the clamp part is the absence of stress concentration because the radius-to-thickness ratio r/e is much larger than unity (see for instance Ref. [13], p. 339).

Finally, the shell of the prototype roll was cut (segmented) every 5 mm using a 0.5-mm thick disc saw in order to reduce pressure crosstalk. It resulted in fifty 4.5-mm large, 56-mm long parallel blades (Fig. 4c). Consequently, the wrap angle should be larger than 20° (0.35 Rad) in order to cover the entire surface of blade.

Fig. 5 shows a cut view of a shell blade and the manufacturing dimensions. Also shown are the locations x_1 and x_2 of the FBGs from both sensing lines SL#1 and SL#2 with respect to the closest clamp position. For the sake of demonstration, only one cylinder hole was transformed into escutcheon. Therefore, the final prototype roll was slightly unbalanced. The prototype roll was left unbalanced because the proof-of-concept was done at small rolling speeds (~ rd/s).

In the following, we describe FE Modelings (FEM) performed as a support for the manufacturing of the prototype roll, according to the second conception. Many books actually treat of analysis of stress/strain on bars and plates [12-14]. Shells are much more difficult to handle mathematically that flat plates [15]. In practice, FEM is used for determining the state of stress/strain of shell blades. We propose a simplified analytical model as well, with variables listed in the nomenclature (table I).

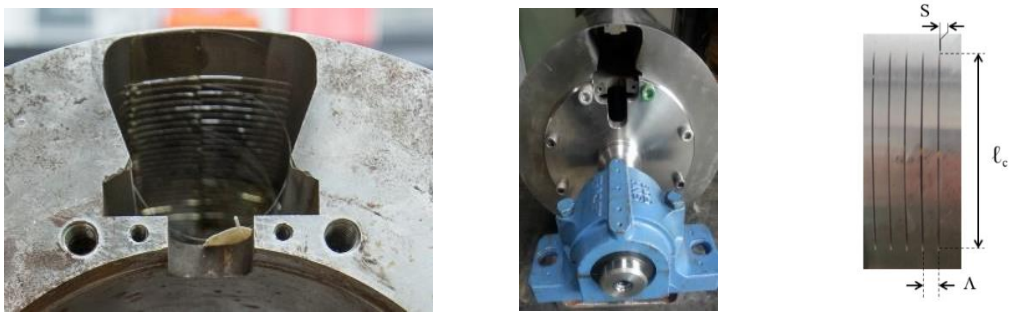

a/ b/ c/

FIG. 4. Views of the prototype roll a/ escutcheon hole, b/ mounted on thrust bearings, c/ shell segmentation (view from top).

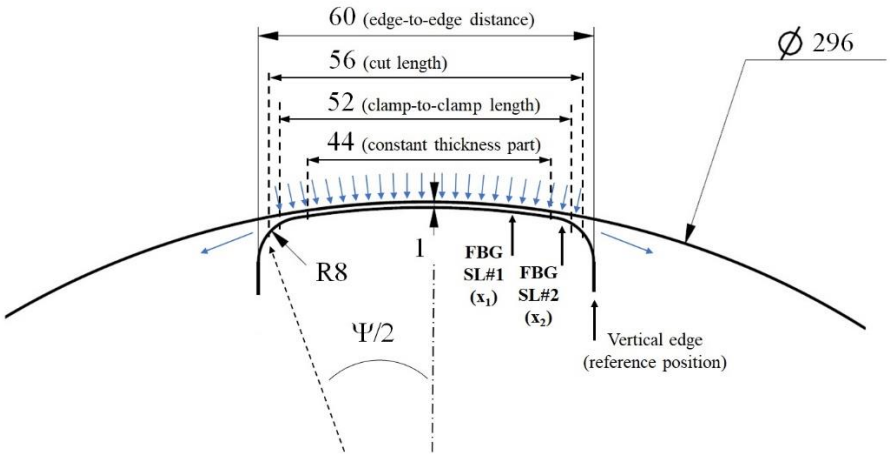

FIG. 5. Section cut along a shell blade showing main manufacturing dimensions.

1. FE modeling (FEM)

We performed FEM of the blades described in Fig. 4 and 5 with the aim to find out where the orthoradial strain reaches its maximum value along the reverse side of the blades machined on the prototype roll (escutcheon hole type). The simulation was done with the software Creo Simulate (PTC Ed.) which is the FE module integrated within Creo Parametric. The software generates polyhedral structures with adjusted polynomial degree depending on required convergence. Convergence was attained because the highest polynomial degree used for building the structure was 5 while the software allows for up to 9.

The shell blades (design value thickness: 1 mm) were uniformly loaded by a steel strip (section = 0.2 x 200 mm^2) under extension by a force of 3000 N and under a wrap angle of 120°. The strip is thus submitted to a tension of 75 MPa and the average contact pressure over the blades (Eq. (3)) is 84 kPa (the total force over a single blade surface is 19.6 N).

Fig. 6a shows the displacement in false color mapping on top side of the blade (in contact with the strip). As expected, the maximum deflection is located at mid-part of the blades and is -25.92 µm.

Fig. 6b shows the strain distribution in false color mapping on the surface of the reverse side of the shell blades. As expected, the maximum strain is located near the clamps, at a distance of about 2 mm from nearest cut end and 4 mm from the nearest edge. The local stress decreases rapidly beyond each clamp due to the rapid increase in local thickness. According to this loading condition, the maximum strain is -211.6 microstrain (43.7 MPa). At x_2, the strain is about -165 ± 10 microstrain (34 ± 2MPa).

Finally, Fig. 6c shows the Von Mises stress distribution along a cut view of a blade that reveals several important things:

_ the loading condition is a combination of compression and bending.

_ the bending moment is maximum near the clamps and at mid-part. The shell blade has therefore the same behavior as a plate with built-in extremities, i.e. the bending moment equals the end-fixed moments $M = F\,\ell/8$ at the clamp position ($x = 0$), it is zero at $x = \ell/4$ and then $M = -F\,\ell/8$ at mid-part ($x = \ell/2$). The bending stress is thus maximum on top of the blades and near clamps on reverse side.

_ As the blades were cut over a distance of 56 mm, we conclude from this modeling that the equivalent length of the blade is about 52 mm ± 1 mm.

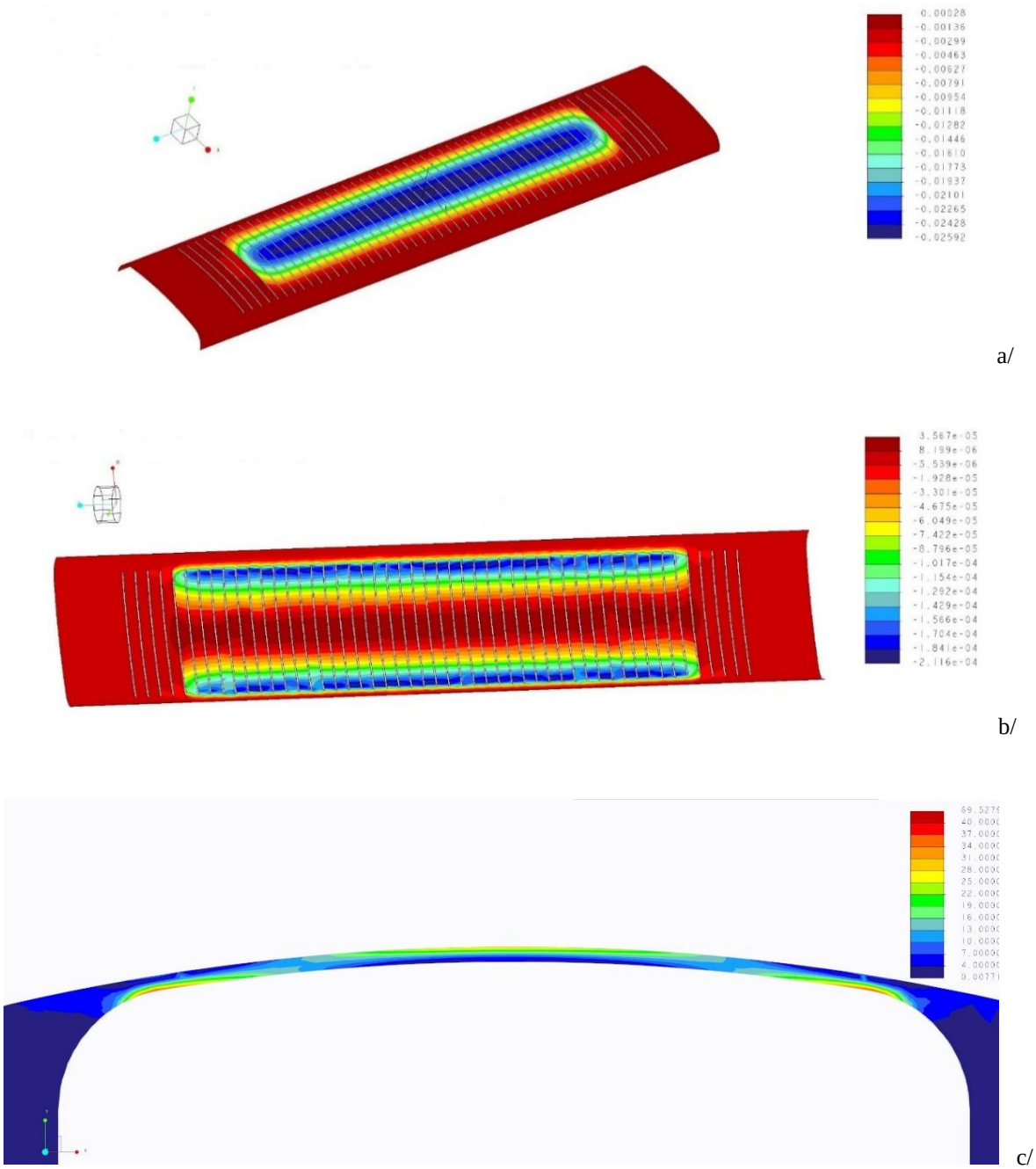

FIG. 6. View in false color mapping of the deflection distribution (a/), surface orthoradial strain distribution (b/) and Von Mises stress distribution along a cross-section of a blade (c/) under uniform strip loading (design value thickness = 1 mm, strip tension = 75 MPa, strip section = 0.2 x 200 mm^2, wrap angle = 120°). The FE modeling was performed by Arcelor-Mittal R&D using Creo Simulate (PTC).

2. Analytical modeling

We propose a simplified analytical model for the blade based upon previous considerations brought by FEM. We first analyze the in-plane stress and then the bending stress.

a/ In-plane stress

Fig. 5 shows that the vertical component of the in-plane reaction force N compensates for the contact force applied on top of the blade [17]. It yields to the equilibrium of force:

$$F = 2 \cdot N \cdot \sin\left(\frac{\Psi}{2}\right), \quad (6)$$

where Ψ is the sensing angle of the roll. In the case of a uniformly loaded blade, the force F acting on a blade writes as:

$$F = P \cdot L \cdot R \cdot \Psi, \quad (7)$$

where L is the width of a blade (not to be confused with the blade period) and R is the radius of the roll.

Since Ψ is small, we consider $\sin\left(\frac{\Psi}{2}\right) \sim \frac{\Psi}{2}$, and equating (6) and (7), it yields:

$$N = P \cdot R \cdot L, \quad (8)$$

Considering a blade thickness e, its cross section is $e \cdot L$ and the in-plane stress within the blade cross-section is therefore [17]:

$$\sigma_c = \frac{N}{e \cdot L} = P \cdot \frac{R}{e}, \quad (9)$$

Given a contact pressure of 84 kPa, the in-plane compression stress σ_c is -12.4 ± 0.6 MPa for a 1-mm thick blade. The in-plane strain is then -60 ± 3 µstrain and the strain-to-load sensitivity is -3.07 microstrain/N. As Eq. (9) does not depend on Ψ, it is assumed to be homogeneous along the blade. This compressive stress value is shown in clear blue in Fig. 6.c.

b/ Bending stress

As shown by FEM, blade shape only affects stiffness while moments are unchanged. We provide here a review of the equations that rule the moments and deflections for a thin plate under concentrated and uniformly distributed loading, as a comparison with FEM of the shell part. Equilibrium relationships for both forces and moments are described in books [12-16].

Since the shell blades are part of the roll structure, they are clamped at each extremity, i.e. each blade is kept in position by end-fixed moments on their left and right sides [13]. Let us consider a concentrated load (local force) F applied at a distance a (a < b) from the nearest clamp at left side, both end-fixed moments write as:

$$\mu_{left} = F \cdot a \cdot (b/\ell)^2 \, , \mu_{right} = F \cdot b \cdot (a/\ell)^2 \, , \quad (10)$$

where ℓ is the blade length (between clamps) and a and b are the distances between the point of application of the force and the left and right clamps respectively ($a + b = \ell$).

In the special case of a local force applied at the middle of the blade, both end-fixed moments equal to the value:

$$\mu_l = F \cdot \ell/8 \, , \quad (11)$$

In case of a uniformly distributed force along the blade length ($p = F/\ell$), both end-fixed moments equal to [13]:

$$\mu_d = F \cdot \ell/12 \, , \quad (12)$$

Finally, reaction moments (reaction forces from clamps) and bending moments due to reaction forces superimpose over end-fixed moments. At last, 6 equations actually rule the shell blade, that is in statically indeterminate configuration (in case the structure is in statically-determinate configuration, only 4 equations are needed) [12-13]-[16].

In the particular case where the FBG is bonded close to a clamp ($x \rightarrow 0$ or $x \rightarrow \ell$), moments due to reaction forces are negligible compared to end-fixed moments. This is because the distance between the clamp and the point of application of the force is small compared to the blade length. In that case, the strain is governed by end-fixed moments and one may notice that the ratio μ_l/μ_d of mid-point *vs* distributed end-fixed moments is 3/2 (i.e. a force applied at mid-point is 50 % more efficient than a distributed load).

TABLE I. Nomenclature.

Description	Symbol	Value	Comments
DIMENSIONAL			
Roll width		300 mm	
Roll radius	R	148 mm	
Blade period	Λ	5 mm	
Blade width	L	4.5 mm	
Saw cut	S	0.5 mm	
Edge-to-edge distance		60 mm	
Sensing angle	Ψ	0.35 rad (1/18 rd)	Between clamps
Blade length	ℓc	56 mm	From cut ends
	ℓ	52 mm	Between clamps
Blade thickness	e	1 mm	Over 44 mm, design value for FEM = 1 mm
Blade surface	s	234 mm^2	Estimated from FEM
Number of blades		50	Sensing length = 250 mm
Clamp-to-FBG distance	x_1	12 mm ± 0.5 mm	FBG from SL#1 bonded at 16 mm from edge
	x_2	4 mm ± 0.5 mm	FBG from SL#2 bonded at 8 mm from edge
Wrap angle	α		
Strip thickness	t		Strip-dependent
Strip width	W		Strip-dependent
MECHANICAL			
Young Moduli			
Steel	E	190 GPa	E335 steel (E' = 207 GPa)
Epoxy	E_e	1.5-2.5 GPa	
Silicone	E_s	0.3 MPa	
Poisson ratios			
Steel	ν	0.29	
Epoxy	ν_e	0.33	
Silicone	ν_s	0.5	
Blade stiffness			
Single blade	K	280 N/mm	Force applied at mid-part of the blade
Equivalent	K'		K_f-dependent
Film stiffness	K_f		Depends on film thickness
Stiffness ratio	ζ		$\zeta = K/K_f$
Sensitivities			
Deflection-to-load	Sl	µm/N	Force applied at mid-part of the blade
Deflection-to-pressure	Sp	µm/kPa	Distributed load along blade length
Bragg-to-load	Σl	pm/N	Force applied at mid-part of the blade
Bragg-to-pressure	Σp	pm/kPa	Distributed force along blade length
Force	F	N	
Pressure	P	kPa	
Deflection	D	mm	
Moments	µ, M	N.m	
Strain	ε	unitless	

Uncertainties			
Sensor	σs	pm	
Flatness (5-I)	σf	pm	5-I = 5 10^{-5}
Coupling coef.	$\Gamma_{j,i}$	unitless	
OPTICAL			
Number of FBG per line		25	
Wavelengths	λ	1519-1589 nm	C+L bands

In the following, we assume that the 3/2 ratio (demonstrated for a flat plate) is still valid for a shell blade because of its sole dependence to end-fixed moments [15]. Since the bending-induced strain is proportional to the local moment (as given by Eq. (13)), this useful tip allows mid-point sensitivity to be converted into distributed sensitivity, as will be shown later.

Let x be the abscissa of the sensor (FBG) along the blade ($x=x_1$ or x_2), the local bending-induced strain $\varepsilon_b(x)$ depends on the moment M(x), according to

$$\varepsilon_b(x) = \frac{y}{E' \cdot I} \cdot M(x) \,, \tag{13}$$

where y is the local distance to the neutral surface, E' is the apparent Young modulus of the blade respectively and I is the quadratic moment (moment of inertia) given by

$$I = L \cdot e^3/12 \,, \tag{14}$$

The apparent Young modulus E' takes into account the increase in stiffness of a plane structure (plate or shell) compared with a bar of near zero width/length aspect ratio. It is written as follows [13]-[15]:

$$E' = E/(1-\nu^2) \,, \tag{15}$$

where ν is the Poisson coefficient of the material (ν = 0.29 for steel). The increase in stiffness is about 9 % for steel blades. The bending-induced stress (that superimposes over the compressive stress σ_c) is then

$$\sigma_b(x) = \frac{y}{I} \cdot M(x) \,, \tag{16}$$

Practically, fiber bonding does not significantly change the quadratic moment of the blade because the added moment due to the fiber is negligible with respect to that of the blade. This is demonstrated by using the composition law for quadratic

moments. This law states that the resulting moment is $I' = I + A.\delta^2$, where I is the quadratic moment of the structure part with respect to its geometrical center, A is its section and δ is the distance between the barycenter of the structure part and the neutral surface of the shell. Let us consider an epoxy thickness of 100 µm, supported by experimental results (see IV.C.1). The quadratic moment of the fiber and epoxy coating (with respect to the mid-part of the blade) are then about $8\ 10^{-5}$ mm^4 and 0.11 mm^4 respectively. As the stiffness is governed by the product EI, the rigidity ratio of the fiber and coating relative to that of the blade are $(EI)_{fibre}/(EI)_{blade} \sim 0.008$ % and $(EI)_{coating}/(EI)_{blade} \sim 0.22$ %.

Near a clamp, the local moment M(x) is equivalent to the end-fixed moment. In the following, we shall consider the strain near the clamp part where the strain is maximum. S. Timoshenko provided a complete analysis of both deflection and stress distributions for end-fixed plates [15]. He introduced a correction parameter $\Psi_1(u)$ (where u is an unitless parameter that depends on reaction force) that accounts for the influence of the moment due to deflection itself (moment due to reaction force from clamp). In our case, this coefficient is close to unity so that we disregard this contribution in the following development.

Let us consider a concentrated load (local force) acting at a distance a (a < b) from the clamp on which the FBG is bonded to. Then, using Eq. (10) and Eq. (13), the bending-induced strain close to the clamp part (i.e. at $x = x_2$) is:

$$\varepsilon_l(x_2) = \frac{y}{E' \cdot I} \cdot F \cdot a \cdot \left({}^{b}/_{\ell}\right)^2 , \tag{17}$$

In the special case of a concentrated load applied at the middle of the blade ($a = b = \ell/2$), Eq. (17) reduces to:

$$\varepsilon_l(x_2) = \frac{y}{8 \cdot E' \cdot I} \cdot F \cdot \ell , \tag{18}$$

Similarly, the bending-induced strain over the clamp part under uniformly distributed loading depends on the end-fixed moment given by Eq. (12), from which we get:

$$\varepsilon_d(x_2) = \frac{y}{12 \cdot E' \cdot I} \cdot F \cdot \ell , \tag{19}$$

From Eq. (18), we get the Bragg-to-load sensitivity (in µstrain/N) in case of mid-part concentrated load (bending only):

$$\Sigma_l \left(\frac{\mu strain}{N}\right) = \frac{\varepsilon_l(x_2)}{F} = 10^6 \cdot \frac{y}{8 \cdot E' \cdot I} \cdot \ell \tag{20a}$$

In case of uniformly distributed loading, the contact pressure is given by P = F/s, where s is the blade surface given by $s = L \cdot \ell = 234\ mm^2$. From Eq. (19), we get the Bragg-to-load sensitivity (in µstrain/kPa) in case of uniformly distributed load (bending only):

$$\Sigma_d\left(\frac{\mu strain}{kPa}\right) = \frac{\varepsilon_d(x_2)}{P} = 10^9 \cdot \frac{y}{12 \cdot E' \cdot I} \cdot \ell \cdot s = \frac{2 \cdot s}{3} \cdot \Sigma_l \quad (20b)$$

The deflection D at mid-part of the shell blade is given by [12-13]:

$$D = \frac{F \cdot \ell^3}{\beta \cdot E \cdot I}, \quad (21)$$

where β is a dimensionless parameter that depends on structure geometry and loading conditions. For straight bars or plates, β values are $\beta_l = 192$ and $\beta_d = 384$ for concentrated load at mid-part or uniformly distributed load respectively [12]. In case of mid-part concentrated loading, we get from Eq. (21) the deflection-to-load coefficient as follows:

$$S_l\left(\frac{\mu m}{N}\right) = \frac{D}{F} = 10^6 \cdot \frac{\ell^3}{\beta l \cdot E \cdot I} = 10^6 \cdot \frac{12 \cdot \ell^3}{\beta l \cdot E \cdot L \cdot e^3}, \quad (22a)$$

In case of distributed loading, the deflection-to-pressure coefficient writes as:

$$S_d\left(\frac{\mu m}{kPa}\right) = \frac{D}{P} = 10^9 \cdot \frac{\ell^3 \cdot s}{\beta d \cdot E \cdot I} = 10^9 \cdot \frac{12 \cdot \ell^4}{\beta d \cdot E \cdot e^3}, \quad (22b)$$

Arcelor-Mittal engineers performed FE modelings with the help of the Abaqus software (Dassault Systèmes, France) of elementary shells (54.5-mm long, 2-mm wide, 1-mm thick) with right-angled clamp connections. These modelings revealed that the β coefficients were $\beta_l = 1034$ and $\beta_d = 2940$ under localized and uniformly distributed loading respectively, evidencing for the stronger stiffness of shell parts compared to straight bars or plates of same width and apparent length. Another important result is that the blade appears stiffer by a factor of 2.84 under distributed loading compared to concentrated loading. It yields:

$$\frac{S_l}{S_d} \cdot s = \frac{\beta d}{\beta l} \sim 2.84 \quad (23)$$

In the following, we get into the details of the fiber deployment inside the roll structure and the FBG readout units that were used during the project.

C. FBG sensing line and associated readout units

We used two FBG readout units during the project.

The first readout unit is a CEA LIST proprietary one. It is based on a compact spectrometer (I-MON-512, Ibsen Co.) equipped with an InGaAs imaging photodetector (Hamamatsu G11620) that covers the spectral range [1510 nm - 1595 nm] with a spectral resolution of 170 pm. It incorporates a broadband ASE (Amplified Spontaneous Emission) source emitting in the range [1510 nm - 1580 nm].

The second readout unit was a compact spectrometer as well (FBG-Scan 704D, FBGS Co.) that may provide up to 4-channel parallel recording within the wavelength range [1525 nm - 1565 nm].

For both readout units, the scan rate is 960 Hz over a single channel. Finally, Bragg wavelengths are estimated from spectra with the help of reconstruction algorithms, assuming that Bragg spectra are not deformed (e.g. chirped) but purely wavelength-shifted. The reconstruction algorithm used by CEA LIST was Gaussian-top. The 1-σ deviation of the Bragg measurement is ~ 0.3 pm at the scan rate of 960 Hz.

The WDM capacity of a FBG readout unit depends on both spectral and strain ranges. Based on a strain range [0 - 1800 microstrain], the expected Bragg shift is -2.2 nm. Therefore, we specified a spectral separation of 3 nm between successive gratings in order to avoid spectral overlap. It yielded a maximum capacity of 25 FBG per optical line for demonstration purpose.

Furthermore, we assume a constant temperature all along the roll profile (at least for the demonstration phase), i.e. no temperature gradient. However, in real conditions, the temperature of the roll is likely to change in time as well all along the roll profile because cold rolling processes involve local heating as flatness control means (in addition to hydraulic actuators). In an industrial context, the spectral separation would probably be larger than 3 nm (e.g. 5 nm) to account for inhomogeneous temperature change.

The singlemode fiber was bend-insensitive and polyimide (PI)-coated. Wavelength-to-position discrimination is achieved by photowriting the FBGs on the fiber strand by increasing order of wavelength, spaced 170 mm apart. The lowest Bragg wavelength was 1518 nm and the highest one was 1589 nm (i.e. FBG#1: 1518 nm, FBG#2: 1521 nm, etc. until FBG#25: 1589 nm).

In order to minimize chirp effects due to strain gradients, short-length gratings were used (i.e. 1.8 mm). The Full Width at Half-Maximum (FWHM) was 0.46 nm and the number of data points used for the Gaussian-top fit was about five.

Each sensing line inside the roll was equipped with a FC-APC connector and connected to a single channel singlemode optical rotary joint (Princetel MJXA-155).

D. Insertion of the Bragg sensing lines into the roll

Two identical sensing lines were incorporated into the prototype roll from each hole entry. A first sensing line (SL#1) was deployed along a first set of 25 blades, leaving enough space on the other side for the placement of a capacitive sensor. Then, one year later, a second sensing line (SL #2) was deployed along the second set.

The operating mode consisted in assembling a tri-cylinder support covered by a thin polyester (PE) film. Each cylinder is 16 mm in diameter to fit inside the round clamp. Firstly, we wrapped the sensing fiber around the PE film. To achieve this, every FBG was kept fixed and aligned perpendicularly to the support axis by applying two dots of instant adhesive (cyanoacrylate) located ± 8 mm apart from it. Secondly, we moved the roll inside an oven with the help of a forklift, with its escutcheon hole down below (Fig. 7).

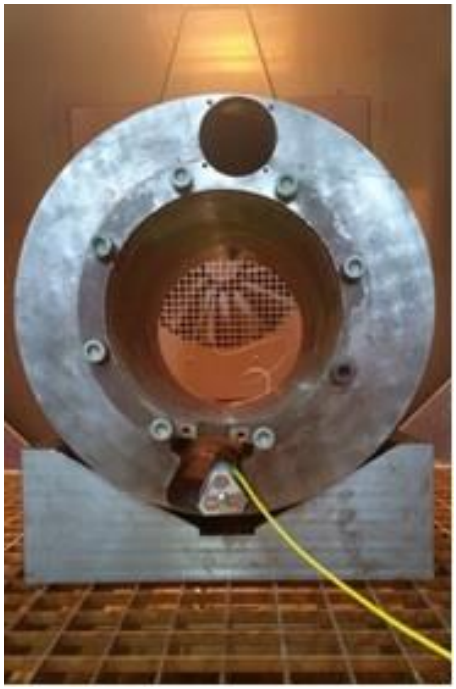

FIG. 7. View of the roll with the escutcheon part down below and the tri-cylinder support for the FBG sensing line.

Then, we covered the FBGs with epoxy resin and the support was turned upside down onto the internal surface of the shell. The support was in contact with the closest edge of the escutcheon hole used as reference point.

As seen in Fig. 8, FBGs from SL#1 were placed at 16 mm ± 0.5 mm from the edge (referring to Fig. 5b) and at 12 ± 0.5 mm from the clamp. FBGs of SL#2 were placed at a distance of about 8 ± 0.5 mm from the edge, i.e. 4 ± 0.5 mm from the clamp.

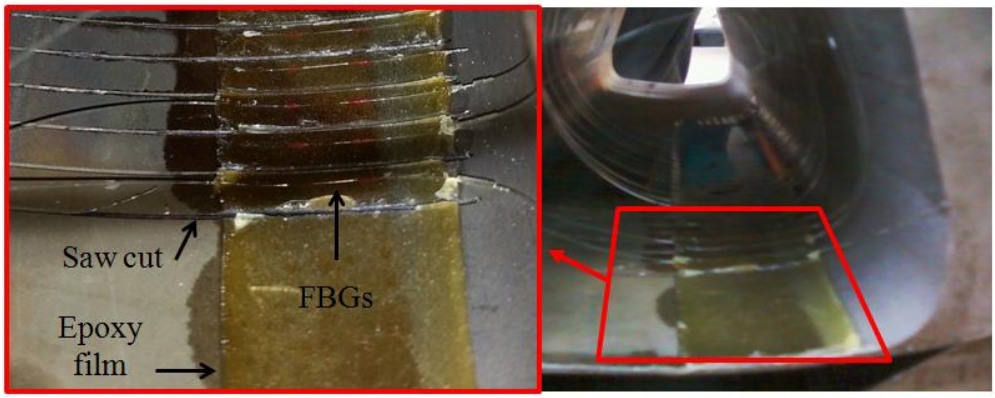

FIG. 8. View of the reverse side of the shell showing the internal part of the blades and the FBGs of SL#1 (localized by red dots) covered by an epoxy film. This photograph was taken after saw-cut of the epoxy film.

Finally, the whole was exposed to a temperature cycle in order to cure the epoxy resin. After curing completion, we moved the roll out from the oven and removed the triaxial support. The polyester film may be eliminated granted that the adhesion of epoxy onto polyester is less efficient than onto steel. In case excess glue leaked out the cut, the external surface of the sleeve is sand-papered. The epoxy film spread out during the heating phase because the surface tension of the epoxy decreases with temperature. An uniform epoxy film is obtained because surface tension predominates over gravity influence (due to the curvature of the internal surface).

The first FBG (#1, 1518 nm) of SL#1 was bonded onto blade #25, located close to the middle of the roll while the last FBG (#25, 1589 nm) was bonded onto blade #1, close to the edge.

The first FBG (#1) of SL#2 was bonded onto blade #24 while the penultimate FBG (#24) was bonded onto blade #1. The last one (FBG#25) was bonded onto the edge of the roll.

The final prototype roll is shown on fig. 9.

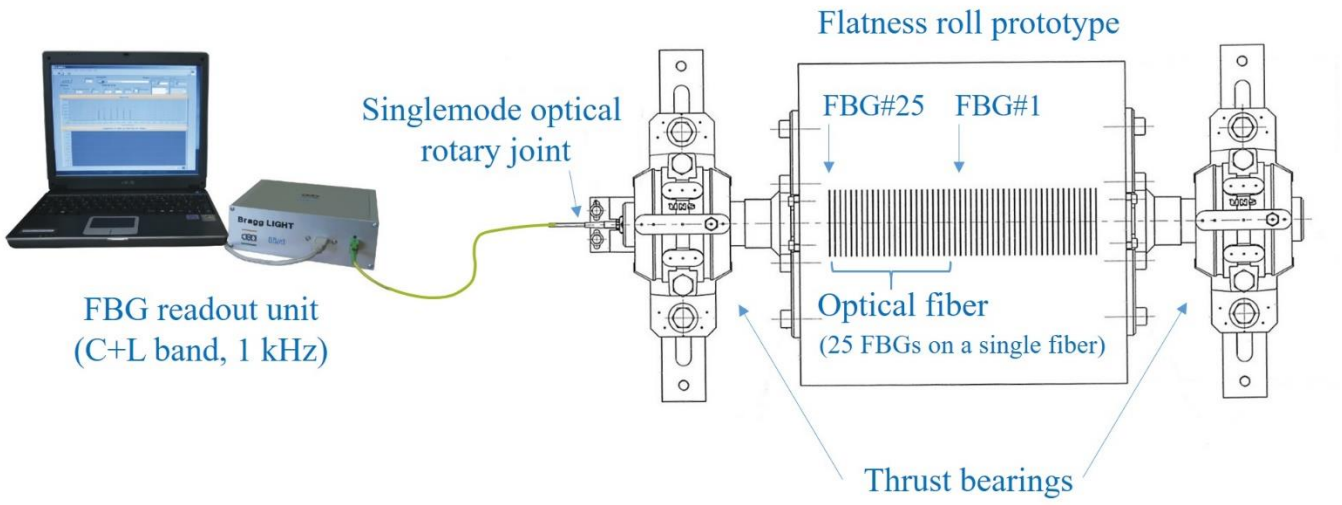

FIG. 9. Design sketch of the prototype roll equipped with FBG strain gauges. Optical signals are extracted from the roll using a singlemode optical rotating joint (SL#1 configuration is shown).

IV. CALIBRATION OF THE FBG PROTOTYPE ROLL

We preliminary investigated blade stiffness and both deflection-to-load and Bragg-to-load sensitivities under both loading configurations. Then, two different calibration procedures for the prototype roll were investigated at Arcelor-Mittal R&D (Maizières-les-Metz, France), either on or off pilot line.

A. Blade stiffness

1. Deflection-to-load sensitivity

a/ Concentrated load: Prior to implementation of SL#2, we mounted a capacitive sensor (Capacitec 220-SLC) inside the escutcheon hole through a slide machined on below part (see Fig. 4a). Then we applied a concentrated load at mid-part of each blade using a tip applicator connected in series with the U1 load sensor (Wagezelle). We recorded the blade deflection at mid-part with respect to the applied load. It yielded a stiffness $K_{exp} = \Delta F/\Delta D \sim 280\ 10^3$ N/m ($\pm\ 3\ 10^3$) for a free blade. It corresponds to a deflection-to-force coefficient Sl = -3.50 µm/N ± 0.03 (e.g. a deflection of -140 µm under an applied force of 40 N).

Taking into account a blade thickness of 1 mm ± 0.05 mm (at mid-part), from Eq. (22a) we get the experimental β_l coefficient $\beta_l \sim 564 \pm 89$. The uncertainty is quite large because the thickness value is placed at the power of three in Eq. (22) (a manufacturing tolerance of 50 µm was considered here). The β_l coefficient is lower than the value obtained from FE modeling (III.A.1) by a factor of ~ 1.8. If we consider the FEM value for β_l (1034) instead, it leads to a deflection-to-load sensitivity of -1.9 µm/N, i.e. about half the measured value.

b/ Uniformly-distributed load: It is worthwhile comparing this result to the FE modeling (Fig. 6) under uniformly distributed load. Using Eq. (3), we get a contact pressure of 84 kPa and a distributed contact force of 19.6 N. The deflection-to-pressure and deflection-to-force sensitivities for the 1-mm thick blade (design value) are then $S_d \sim -0.31$ µm/kPa (-25.92 µm/84 kPa) and -1.32 µm/N (-25.92 µm/19.6 N) respectively.

Following Eq. (22b), we get $\beta_d \sim 1489$. Here again, the β_d coefficient is smaller than the β_d calculated with Abaqus (2940). A possible reason for this is that the blades are connected to the roll structure with rounded clamps instead of right-angled clamps therefore bringing additional flexibility. The ratio β_d/β_l is then 2.64 ± 0.36 in accordance with the value of 2.84 obtained by FE modeling within experimental uncertainty that is quite large due to manufacturing tolerance of the blade thickness (that is amplified due to the power-of-3 dependence).

Finally, it is worthwhile estimating the deflection-to-load sensitivity under mid-part concentrated load, deduced from the deflection-to-pressure obtained from FE modeling. Eq. (23) may be rewritten as:

$$S_l\left(\frac{\mu m}{N}\right) \sim 2.64 \cdot \frac{S_d\left(\frac{\mu m}{Pa}\right)}{s(m^2)} \sim 2640 \cdot \frac{S_d\left(\frac{\mu m}{kPa}\right)}{s(mm^2)} \quad (24)$$

It yields a deflection-to-load sensitivity S_l ~ -3.48 µm/N ±0.48, in agreement with the experimental value (-3.5 µm/N ± 0.03).

2. Bragg-to-load sensitivity

The stress on the reverse side of the blade is the combination of compressive stress and bending stress: $\sigma = \sigma_c + \sigma_b$.

In III.A.1 and III.A.2 we calculated the strain on the surface of the 1-mm thick steel blade. In order to infer the strain within the optical fiber, we first assume a strain-transfer ratio close to unity [18-19]. This assumption is reasonable because the bonded length is typically 20 to 25 mm long (see Fig. 8). Furthermore, FBGs are photowritten inside the fiber core that is at least about 75 µm away from the steel surface (outer polyimide coating ~ 150 µm). As a result, the fiber is located further from the neutral surface and the bending strain in the fiber core is higher than the bending strain on steel surface by a factor 2y/e = 1 + Ø/e where Ø is the outside diameter of the PI-coated fiber. The factor is 1.15 for e = 1 mm.

a/ Concentrated load: The in-plane stress under concentrated load is identical to that under distributed loading and the strain-to-load is the same (-3.07 microstrain/N). From Eq. (20a), the strain-to-load sensitivity (due to bending) is~ -48 ± 4 µstrain/N for a FBG bonded onto the clamp part (y= Ø/2 + e/2). The total strain (compression + bending) is thus -52 ± 4 µstrain/N. Translated into Bragg shift (1.21 pm/µstrain), it yields an expected Bragg-to-load sensitivity of -63± 5 pm/N for a FBG bonded onto the clamp (x = 0). Here again, the uncertainty is quite large due to uncertainty in thickness (that is amplified due to the power-of-2 dependence).

In Fig. IV.4, we recorded Bragg shifts of FBGs bonded onto liberated blades ($x = x_2$) with the readout unit of CEA. It yielded Bragg-to-load sensitivities of typically ~ -55 pm/N ± 5, in accordance with the analytical evaluation (granted that the FBG of SL#2 are bonded at x_2 = 4 mm).

b/ Uniformly-distributed load: We have shown that the uniformly distributed loading configuration is 2/3 less efficient than mid-point concentrated loading for a FBG bonded onto the clamp part (see Eq. (20b)). Consequently, we expect a Bragg-to-

load sensitivity of -42.3 ± 3 pm/N (2/3· 63) under uniformly distributed loading based on Bragg-to-load sensitivity under mid-part concentrated loading.

Applying Eq. (20b) leads to a strain-to-pressure sensitivity of -7.5 ± 0.8 µstrain/kPa onto clamp part due to bending (the factor 1.15 is considered). According to FEM (III.A.1), the strain due to the in-plane compressive stress is -60 ± 3 µstrain for a contact pressure of 84 kPa. The strain-to-pressure sensitivity due to in-plane stress is then -0.71 ± 0.04 µstrain/kPa. The total strain-to-load sensitivity (bending + compressive stress) is then -8.2 ± 0.8 µstrain/kPa. Translated into Bragg shift, we obtain a theoretical Bragg-to-pressure sensitivity of -9.9± 1.2 pm/kPa for a FBG that would be bonded onto the clamp part (x = 0), where the stress is maximum.

We shall now reconsider the FEM (III.A.1) of the 1-mm thick blade. Under the appliance of a contact pressure of 84 kPa, we got a maximal surface strain of -211.6 microstrain at the clamp position (~ -165 ± 10 microstrain at $x = x_2$). Part of this strain is due to compression (-60 ± 3 µstrain) and the remaining part due to bending equals -151.6 ± 3 µstrain (~ -105 ± 13 µstrain at $x = x_2$). Applying the factor 1.15 to the bending-induced strain, it means that the total strain in the fiber is -234 ± 3 µstrain (~ -181 ± 18 µstrain at $x = x_2$). It follows that the strain-to-pressure sensitivity is -2.78 µstrain/kPa, (-2.15 ± 0.22 µstrain/kPa) which translates into a Bragg-to-pressure sensitivity of -3.36 pm/kPa (-2.61 ± 0.27 pm/kPa).

As the resultant force applied by the strip onto a blade is about 19.6 N ($s = 234\ mm^2$), the strain-to-load sensitivity is then -11.94 ± 0.15 µstrain/N (-234 ± 3 µstrain/19.6 N) at the clamp and -9.23 ± 0.9 µstrain/N (-181 ± 18 µstrain/19.6 N) at $x = x_2$. It translates into -14.5 ± 0.2 pm/N at clamp part and -11.2 ± 1.1 pm/N, i.e. three times smaller than expected (-42.3 pm/N).

As a conclusion, both analytical calculation and FEM and in accordance with experimental deflection-to-load sensitivities. Experimental Bragg-to-load and Bragg-to-pressure sensitivities are also in accordance with analytical calculations but are three times higher than those deduced from FEM (we performed several modelings with distinct loading parameters but it led to the same conclusions). In the calculation, we assumed that the fibre was in contact with the steel surface. However, Fig. 7 shows that the thickness of the epoxy layer was of the order of 100 µm to 150 µm and therefore a small steel-to-fibre epoxy gap of several tens of micrometres is likely to appear, but still insufficient to account for such discrepancy. Another source of deviation between FEM and experimental results might be the important stress gradient in this part of shell that amplifies variations in response due to manufacturing tolerance of the blade thickness (~50 µm) but here again the change in Bragg-to-load sensitivity is not expected to be higher than ± 10 %. The most probable explanation to this deviation is that the pressure distribution within the contact is not flat (figure-of-M shape). This is revealed by high stress gradients at the entrance and exit parts of the strip. In

this case, the contact pressure at mid-part on blade surface (and consequently the surface strain) are lower than the average value calculated using Eq. (3). This may account for the underestimation of Bragg-to-load sensitivity by the FEM compared to experimental and analytical calculations.

Experimental, analytical and FEM-based sensitivities are summarized in table II.

TABLE II. Absolute deflection/Bragg-to-load and Deflection/Bragg-to-pressure sensitivities for a 1-mm thick blade shell (manufacturing tolerance ~ ± 50 µm) and FBGs bonded at $x = x_2$. Data in parenthesis are deduced from other data (see text for comments).

Sensitivity	Loading configuration	Analytical ($x = 0$)	FEM ($x = 0$)	FEM ($x = x_2$)	Experimental ($x = x_2$)
Deflection-to-load (µm/N)	Concentrated at mid-part		(-3.48 ± 0.48)		-3.50 ± 0.03
Deflection-to-pressure (µm/kPa)	Uniformly distributed		-0.31		
Bragg-to-load (pm/N)	Concentrated at mid-part	-63 ± 5	(-14.5 ± 0.2)	(-11.2 ± 1.1)	-55 ± 5
Bragg-to-pressure (pm/kPa)	Uniformly distributed	-9.9 ± 1.2	3.36	-2.61 ± 0.27	-7.2 ± 1

B. Dynamic characterization of the flatness roll

Prior to the dynamic test on rolling line, another static calibration was done with an indentation setup at Arcelor-Mittal R&D (Maizières, France). A concentrated load was applied on top of blades and the Bragg wavelengths were recorded with the FBGS 704D reader. An average Bragg-to-load sensitivity of about 4.4 ± 0.5 pm/N was obtained. This value may be converted into Bragg-to-pressure sensitivity using Eq. (20b) and we get 0.68 ± 0.08 pm/kPa $(4.4 \cdot 2s/3)$. We observed a strong inter-blade crosstalk (between 40 % and 60 %) due to the epoxy film that explains why the Bragg-to-load sensitivity is higher when all blades are simultaneously loaded by a strip compared to when the load is concentrated onto a single blade.

Then, dynamic line calibrations were performed with SL#1 on a packaging pilot line at Arcelor-Mittal R&D. Engineers from AM R&D mounted the prototype roll (equipped with SL#1) onto the packaging pilot line, illustrated on Fig. 10. Only the uncoiler capability was used.

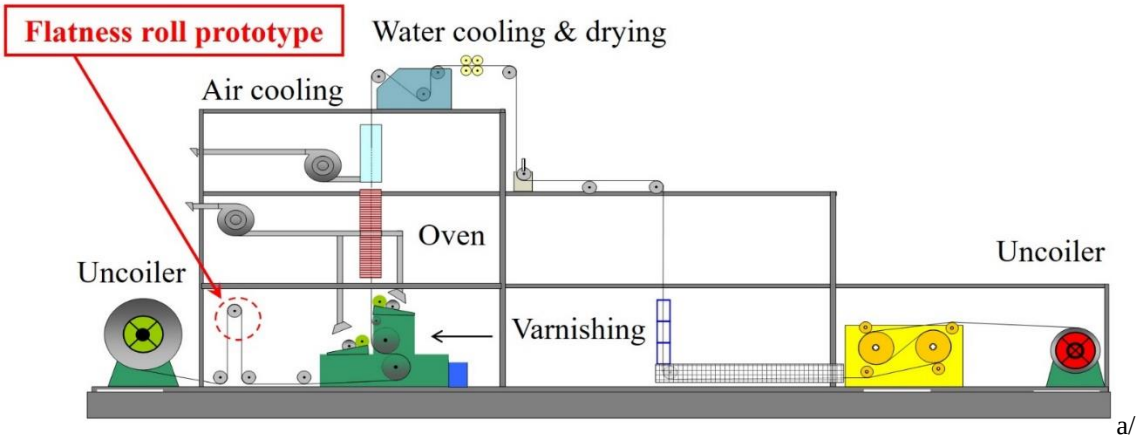

a/

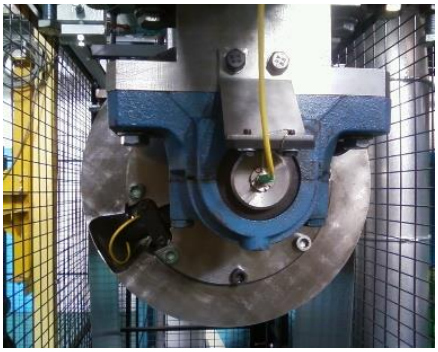

b/

c/

FIG. 10. Description of the packaging pilot line of AM R&D (a/) and view of the prototype roll with its optical rotary joint (b/) and covered by a steel strip (c/).

Two steel strips were tested. The first one was zinc-plated ($0.3 \cdot 215\, mm^2$) while the second one was tin-plated ($0.2 \cdot 200\, mm^2$). The wrap angle was 180°. The roll turned clockwise according to Fig. 10 and the FBGs were mounted on the clamps that enter/leave first the contact.

Each strip was unwind and rewind each time. Both steel strips were tested at several linear speeds (10 m/min, 30 m/min, 60 m/min) and at several pulling forces (noted in kilogramforce - kgf) expressed as a percentage of the maximum pulling force (300 kgf). The rotation rates were 0.179 rd/s, 0.537 rd/s and 1.074 rd/s for 10 m/min, 30 m/min and 60 m/min respectively. From Eq. (3), the maximum contact pressures were 64 kPa and 60 kPa for the tin-plated and zinc-plated strips respectively.

The pulling force was controlled by progressively braking the uncoiler. Without breaking action, a minimum pulling force of 15 % of 300 kgf (45 kgf) is necessary to compensate for friction forces inside the circuit line.

Only 22 FBGs (FBG#4-25) were monitored because the first three gratings delivered poor signals (the power spectral density of the source was too low in this spectral band). The zinc-plated strip had built-in internal stress that yielded scattered strain signals. We then performed strain-to-force calibration with the tin-plated strip that provided more repeatable results along its length. The strip was in contact with the roll from blade #6 (as seen in Fig. 10-c). Blades #1-to-#5 (i.e. FBG#21-to-#25) were not covered by the strip and were only submitted to stress coupling by blade #6.

Fig. 11 shows a typical strain variation as the roll was driven by the tin-plated strip at a rotation rate of 0.179 rd/s (i.e. a linear speed of 10 m/min). We show arbitrarily the strain signal from FBG#5 as example but the other FBGs provided similar results. The reference in strain measurement is recorded while the strip is off-contact. When the strip gets in contact with the blade, the contact pressure deforms it and the strain is coupled to the FBG bonded on reverse side. The difference between the in-contact and off-contact Bragg shift data is proportional to the contact pressure. Temperature compensation is inherently achieved because temperature changes much more slowly than the rotation period of the roll.

Fig. 11 shows bending-induced strain and release peaks that are due to abrupt change in shape imposed by the roll. The roll structure brings energy to the strip in a very short amount of time therefore generating intense positive strain peaks. Conversely, this energy is given back to the roll when the strip is released, thus generating large negative strain peaks (compression). The graph also shows that strain signals are more stable when the shell enters the contact rather than when it comes out. This may be due to friction-induced perturbations that are dominant at the entrance part where equilibrium is not yet achieved.

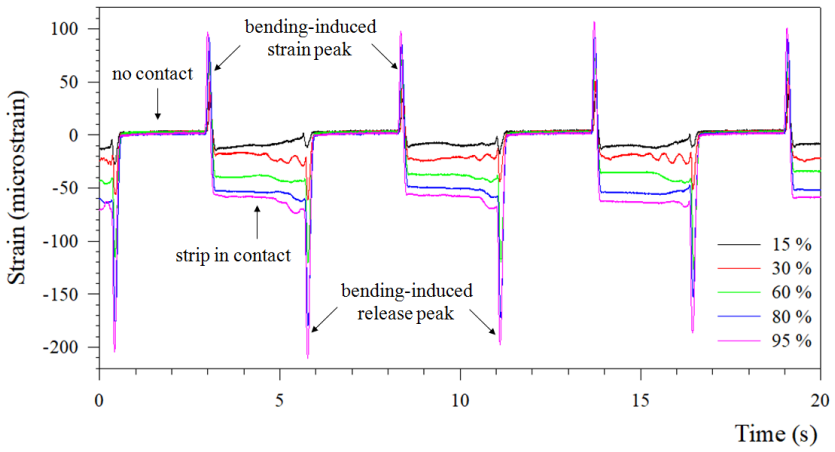

FIG. 11. Example of strain signals obtained with a single FBG (FBG #5) from SL#1 during rotation of the prototype roll on the packaging pilot line (0.179 rd/s, 10 m/min) and for several percentage of pulling force. The tin-plated strip was used.

Fig. 12 shows the pressure patterns post-processed from Bragg shifts, with the help of calibration coefficients obtained from averaged data at low speed (10 m/min), from Fig. 13. Diabolo-shaped pressure patterns indicate that the contact stress oscillated slightly during rolling. The closer to the middle of the strip, the smaller the pressure variations. Compared to data from Fig. 12b and c, Fig. 12a reveals that pressure variations are smaller at lower speed as well. Data from Fig. 12a were averaged over a large number of contacts in order to reduce statistical uncertainty in pressure sensitivity. 1-σ deviations range between ± 1 kPa up to ± 6 kPa for 15 % and 100 % pulling force respectively. The uncertainty in pressure measurement is larger than the expected theoretical uncertainty (0.5 kPa) because is it actually dominated by periodic fluctuations in tensile stress along the strip width.

Fig. 13 shows the Bragg shifts for FBG# 4-25 plotted with respect to pulling forces in the range [45 kgf – 300 kgf]. Bragg shifts linearly change with pulling force (i.e. with contact force), as expected. The mean value for the sensitivity is 0.27 ± 0.04 pm/kgf. However, it is worthwhile noticing that fit curves do not cross through the zero point. For all blades covered by the strip, the residual spectral shift is negative (typically several pm) whereas it is positive for blades placed outside the strip and only submitted to stress coupling. This effect is probably due to the traction force exerted by the strip onto the roll surface that counteracts pressure effect. Sensitivities in pm/kgf are finally translated into pm/kPa with the help of Eq. (2) and Eq. (3).

For the second steel strip (the tin-plated one) and according to the configuration described in Fig. 10, we used the relation:

$$\Sigma_p\left(\frac{pm}{kPa}\right) = \left[4.69 \cdot \left(\frac{kgf}{kPa}\right)\right] \cdot \Sigma_f\left(\frac{pm}{kgf}\right), \qquad (25)$$

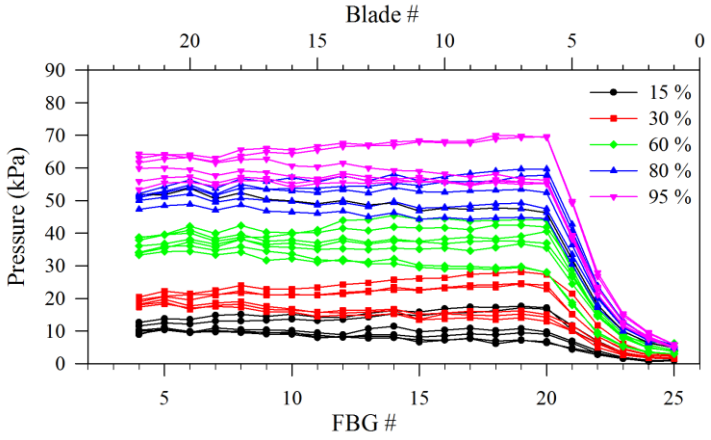

a/

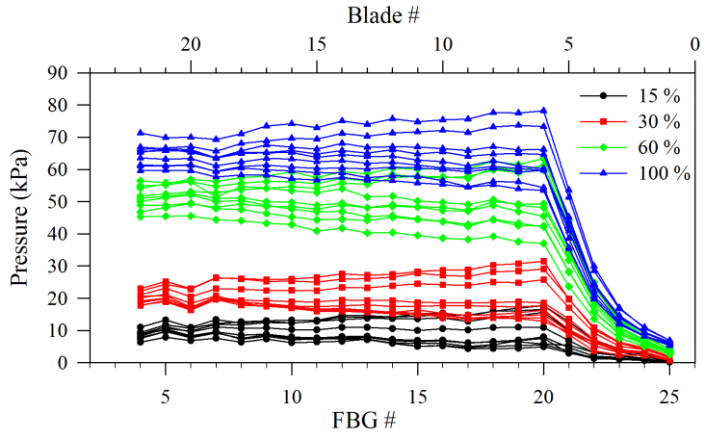

b/

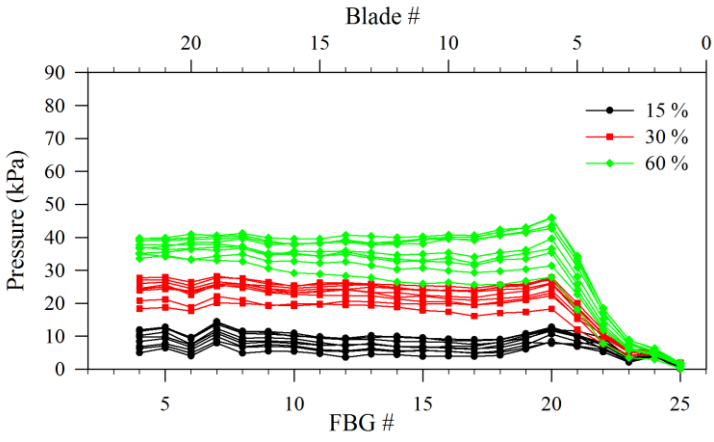

c/

FIG. 12. Pressure patterns post-processed from Bragg shifts recorded with the tin-plated strip during test of the prototype roll on the pilot packaging line at several pulling force ratios *vs* 300 kgf (a/ speed = 10 m/min, b/ speed = 30 m/min, c/ speed = 60 m/min).

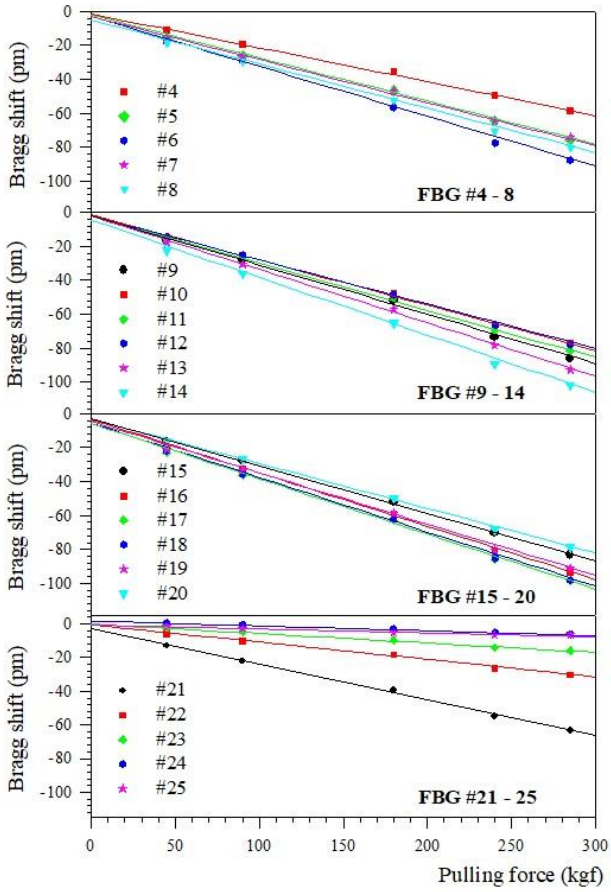

FIG. 13. Pressure-induced Bragg shifts plotted with respect to pulling force for all FBGs of SL #1 (FBG#4-25). FBG#25 is located at the edge of the roll while FBG#1 is located at the middle. The tin-plated strip was used for calibration (data from Fig. 11a).

Fig. 14 shows the calibration chart for SL#1, associated with the histogram of sensitivities tentatively fitted by a Gaussian distribution. Blades #1-5 (FBG#21-25) were out of strip and therefore only submitted to stress crosstalk from blade #6. Therefore, pressure sensitivities for #1-5 (FBG#21-25) were recovered from stress coupling with the help of the coupling model described in the next paragraph.

The mean value for the pressure sensitivity is -1.29 pm/kPa and the 1-sigma deviation is ± 0.2 pm/kPa (Fig. 14). The deviation is due to fluctuation of position of the FBGs along the fiber support and to manufacturing tolerance of the blade. Comparing the mean force sensitivities obtained by load sensing with the indentation setup (4.4 ± 0.5 pm/N) with the mean pressure sensitivities obtained on pilot line (-1.29 ± 0.2 pm/kPa), a conversion coefficient of 3.28 ± 0.13 kPa/N is found for SL#1. This result is half the expected value of 2/3s = 6.4 kPa/N because blades are interconnected by the epoxy film (the equivalent surface

is then higher than the blade surface). Said differently, the mean Bragg-to-pressure sensitivity obtained on the pilot line when all the blades are simultaneously loaded by the strip is twice that measured onto a single blade with the indentation setup.

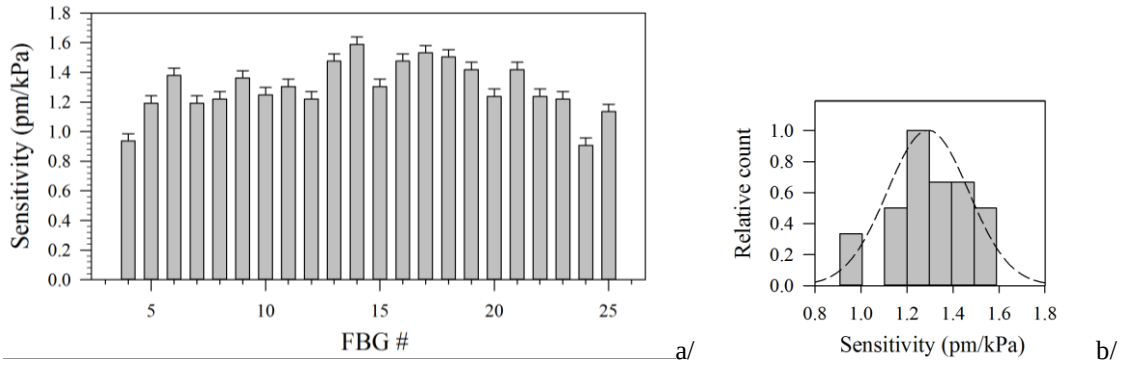

FIG. 14. Calibration chart for SL#1 (in pm/kPa), as obtained from the packaging pilot line at AM R&D at the speed of 10 m/min (a/) and histogram of sensitivities (b/). FBG#25 is located at the edge of the roll while FBG#1 is located at the middle (see Fig. 8).

Finally, Fig. 15 illustrates a sequence of pressure patterns recorded as the roll was driven by the second strip (zinc-plated) at a rolling speed of 60 m/min and under a pulling force ratio of 30 %. Interestingly enough, the pressure pattern moves from left to right as the roll turns. One can see that the pressure pattern showed great dispersion that explains why it the zinc-plated strip was not used for calibration purpose. Several factors account for these large pressure variations, either internal constraints within the strip (from manufacturing and storage conditions) or eccentricities in strip mounting.

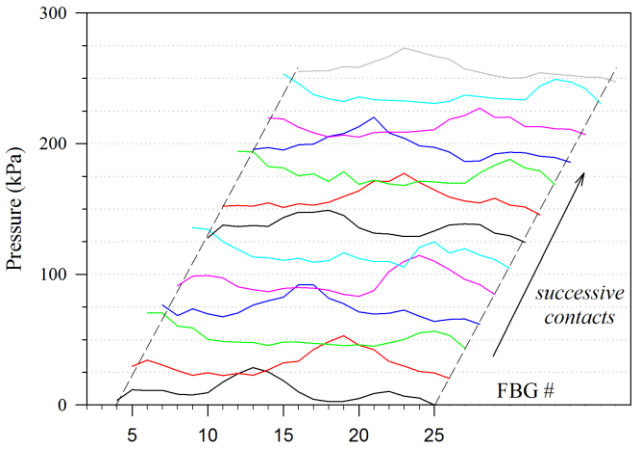

FIG. 15. Example of 3D pressure pattern plots obtained with the zinc-plated strip on the packaging pilot line at AM R&D (rolling speed = 60 m/min, pulling force ratio is 30 %). Plots are shifted upwards by 25 kPa for sake of clarity.

C. Analytical model of stress coupling (“crosstalk”)

We identify two contributions for stress coupling.

The first contribution is an indirect stress coupling ("indirect crosstalk") from one blade to another that comes from reaction by clamps. Although blades are separated by saw-cut they are both clamped to the roll structure which transmits part of the reaction force. The deflection experiment (IV.A) led to the important conclusion that the deflection of nearby blades was 0.8 µm for a force of 40 N, which is fortunately small in comparison with the deflection of the loaded blade (140 µm). Therefore, the indirect crosstalk is typically about 0.6 % and limited to neighboring blades. It may be eliminated by inverse matrix calculation.

In addition to this, the fiber implementation process appears yet unsatisfactory because the epoxy layer re-establishes a direct stress coupling ("direct crosstalk") that was relieved by cutting the blades during manufacturing phase. As evidenced in IV.B, the amplitude of epoxy-induced direct crosstalk is typically 40 % to 60 % and extends away over five or six blades (i.e. ten to twelve blades on both sides). It has the effect of averaging out pressure over nearby sensors, thereby degrading spatial accuracy. Saw-cut of the epoxy film is therefore a prerequisite in order to eliminate direct stress coupling.

However, this is not the only issue to deal with as water tightness of the inner part of the shell must be guaranteed as well in view of a future industrial use. Oil or water ingress must be prevented from deteriorating both the epoxy layer and fiber coating. Soft polymers (such as silicone) may be used as sealants for this application, in order to fill the cuts once again while keeping the direct stress coupling to a value that may be managed by inverse matrix calibration.

In the following, we propose an analytical model of the stress coupling. It is used, first for correcting the crosstalk influence on measurements with SL#1, second to predict the influence of a silicone undercoating on the crosstalk figure and, third for correcting for crosstalk influence with the help of a matrix inversion calculation.

1. Analytical modeling of the rigidity of a polymer film

Let us consider the equilibrium of forces applied onto a pair of blades connected by a polymer film (Fig. 16).

We assume linear static mechanics. The blades are supposed to remain parallel to each other (i.e. no twist). This assumption relies upon the value of the ratio of longitudinal vs transverse stiffness of a blade that is proportional to the square of its aspect ratio, i.e. 1/16.

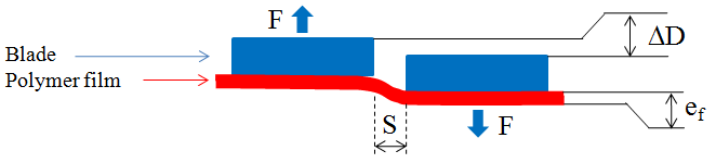

FIG. 16. Sketch of two parallel blades connected by a polymer film bonded onto reverse side and providing clamped boundary condition.

The stiffness of a polymer film is provided by the model of a fixed beam (polymer film) bonded and clamped onto two support plates (blades), with one support that "sinks" with respect to the first one. In this case, the force applied to both blades F is linked with the relative vertical displacement ΔD between both blades by the relation [14]-[16]:

$$F = 12 \cdot \frac{E_f \cdot I_f}{S^3} \cdot \Delta D \,, \tag{26}$$

where S is the width of the saw used for cutting the blades, E_f and I_f are the Young modulus and the quadratic moment of the polymer film respectively (I_f is given by Eq. (10)). The Poisson coefficient of epoxy is 0.33.

The stiffness K_f of the polymer film is then:

$$K_f = 12 \cdot \frac{E_f \cdot I_f}{S^3} \,, \tag{27}$$

In practice, the stress is not limited to the unbonded part of the polymer but rather extends down into the bonded part due to its elasticity. Therefore, the value of S is expected to be much larger than the saw width; a value of 1 mm was considered. E_f ranges between 1.5 GPa and 2.5 GPa according to chemical formulation and curing procedures. A modulus of 1.5 GPa was considered because the epoxy was cured at elevated temperature (~ 100°C) [20].

Stiffness values for the epoxy film that best fit experimental data are estimated to be about K_f = 1280 N/mm for SL#1 and K_f = 636 N/mm for SL#2. Surprisingly, the epoxy film appears to be much stiffer than the metal blade, contributing to a strong direct stress coupling. We explain this counter-intuitive result by the small value of the S-parameter that is placed at the power of 3 and has therefore great impact on the calculation. Although main parameters are not accurately known, a satisfactory correspondence was found between theory and experiment taking into account previous values, with a bond length of 25 mm and thicknesses of 140 µm and 110 µm for the epoxy layers of SL#1 and SL#2 respectively.

2. Analytical modeling of stress coupling

In the following, we consider a vertical force applied onto a single blade. Relative deflections with respect to the loaded blade (blade #0) are calculated using force equilibrium relations and strains are deduced from deflections (using Eq. (21)). The extension of this model to a distribution is possible thanks to superposition principle (we assume linear elasticity for both steel and polymer materials).

Let us consider the equilibrium of force between blade #0 and the other blades placed aside from it. We considered several cases: reaction from a single side, reaction from both sides (assuming symmetry with respect to blade #0), only one single blade connected, two blades connected etc.

Let D_0, D_1, … D_i be the deflections of blade #0 (the loaded one), blade #1, and the i^{th} blade respectively, the force F applied onto blade #0 is balanced by both its own stiffness and reaction from neighboring blades (via K_f).

For blade #0, it yields

$$F = K \cdot D_0 + 2K_f \cdot (D_0 - D_1) \qquad (2 - side)$$

$$F = K \cdot D_0 + K_f \cdot (D_0 - D_1) \qquad (1 - side)$$

Posing $\zeta = K/K_f$ and solving for D_1/D_0 we get

$$D_1/D_0 = (2 + \zeta)/2 - \frac{1}{2K_f} \cdot \frac{F}{D_0} \qquad (2 - side)\,, \tag{28a}$$

$$D_1/D_0 = (1 + \zeta) - \frac{1}{K_f} \cdot \frac{F}{D_0} \qquad (1 - side)\,, \tag{28b}$$

Blade #1 then transmits a force to higher-order blades. Considering blade #1, both the rigidity of blade #1 and the reaction force from blade #2 balance the force (due the imposed deflection onto blade #0). It writes as

$$KD_1 + K_f \cdot (D_1 - D_2) = K_f \cdot (D_0 - D_1)\,, \tag{29}$$

Solving for D_2/D_0, we get:

$$D_2/D_0 = (2+\zeta)\cdot D_1/D_0 - 1\,, \tag{30}$$

Equation (30) is the starting point of a recurrence relation used for calculating all Di/D_0 from previous relative deflections. As a general form, we write:

$$D_i/D_0 = (2+\zeta)\cdot D_{i-1}/D_0 - 1\,, \tag{31}$$

Eq. (28) and (31) provide the relative deflections as a function of the parameter F/D_0 related to blade #0. All reactions forces exerted by connected blades balance the force applied onto blade #0. The equilibrium leads to:

$$F/D_0 = K' = K\cdot\left(1+2\cdot\sum_i D_i/D_0\right) \quad (2-side)\,, \tag{32a}$$

$$F/D_0 = K' = K\cdot\left(1+\sum_i D_i/D_0\right) \quad (1-side)\,, \tag{32b}$$

where K' is the equivalent stiffness for the loaded blade (blade #0) in connection with nearby blades by the polymer film. The ratio K'/K provides an estimation of the amount of stress coupling and subsequent reduction in strain sensitivity.

Eq. (32) is a closure relation that enables to solve Eq. (28) and (31) for D_i/D_0. To do so, values for Di/D_0 are first plotted with respect to increasing values for F/D_0 using Eq.(28) and (31). Then, values for F/D_0 are plotted as well using Eq. (32) with respect to values for D_i/D_0 calculated previously. It yields another linear relation with decreasing values for F/D_0.

The solution for the global equilibrium of blades is given by the intersection coordinates of both F/D_0 relations, yielding all in a row the value of K' and associated values for Di/D_0.

Partially-connected blades on one side are neither 1-side nor 2-side and requires a special treatment as boundary conditions are different. For instance, let us consider blade #-n near the cut. For any value of n, Blade #-n is not connected to blade #-n-1 and therefore Eq. (29) is re-written as follows:

$$KD_{-n} = K_f\cdot(D_{-n+1} - D_{-n})\,, \tag{33}$$

which yields the value of D_{-n} relative to D_{-n+1}:

$$D_{-n} = D_{-n+1}/(1+\zeta)\,, \tag{34}$$

In the special case n = 1, Eq. (34) writes as:

$$D_{-1} = D_0/(1+\zeta)\,, \tag{35}$$

For $n \neq 1$, D_{-n} is used as input data for Eq. (31) and (32).

As immediate use-case, we applied the coupling model to decouple strain data recorded during the on-pilot calibration test. A ζ-value of 0.22 ± 0.02 gave the best adjustment with average values. The equivalent rigidities K' are 1227 N/m and 753 N/mm for 2-side and 1-side cases respectively. The experimental coupling vector [0.23, 0.41, 0.67, 1, 0.73, 0.37, 0.19] was adjusted by the 2-side symmetric vector: [1, 0.63, 0.4, 0.25, 0.16, 0.1].

The coupling model enables us to recover the pressure sensitivities of the blades #1-5 that were out of strip contact (corrected sensitivities are shown in Fig. 14).

D. Static characterization of the flatness roll

In view of the final test on a cold rolling mill at Constellium C-TEC premises with the second sensing line (SL#2), the epoxy layer was cut using a 0.5-mm thick disc saw through existing cuts into steel. Unfortunately, the optical fiber was cut between blade #17 and blade #18. We then decided to stop the cutting process because it was still possible to interrogate the whole sensing line through both extremities. At this stage, blades #1-to-17 were separated while blades #18-to-#25 were still linked by the epoxy film.

Then, off-pilot (static) line calibration was performed with SL#2. This second calibration procedure makes use of a point applicator connected in series with a load sensor (HBM UR1), as shown in Fig. 17.

FIG. 17 View of the calibration experiment at AM R&D involving a load sensor.

We used the readout units described in III.C. The readout unit from CEA monitored FBG#8-25 (related to blades #0-17) while the other readout unit (FBGS) monitored FBG#1-7 (related to blades #18-24).

We loaded the blades at a distance of 17.5 mm from edge (13.5 mm from nearest clamp). Bragg wavelengths were recorded with respect to load in the range [0 - 30 N] and force sensitivities were then determined for each blade. We recorded Bragg-to-load sensitivities of about 46 ± 5pm/N and about 10 ± 2pm/N for liberated blades and connected blades respectively. Compared with SL#1 (IV.B), the sensitivity of connected blades is three times higher due to the placement near the clamp.

Before determining the sensitivity vector for all blades, we first recover the sensitivities for blades #18-25 as if they were saw-cut, with the help of the coupling model (Cf. IV.C).

1. Experimental stress coupling

The crosstalk behavior due to the epoxy layer was estimated from the Bragg wavelengths recorded from FBG#2-7 (blades #18-23). Granted that Bragg wavelength shifts are proportional to strain (1.21 pm/μstrain), relative strain data are equivalent to relative Bragg shifts.

Let us consider the coupling ratio Γj-i, where i refers to the stressed blade and j refers to the connected blade. By definition, we get

$$\Gamma_{j,i} = {}^{\varepsilon_j}/_{\varepsilon_i}\,, \tag{36}$$

As an example, strains experienced by the blades #18-to-#24 are plotted in Fig. 18a, while the load was applied onto blade #18. Coupling ratios Γj,i are shown on Fig. 17b with blade #18 as loaded blade. Instabilities in strain coupling are observed with some blades. Epoxy viscoelasticity is not involved since no hysteresis is observed. It may be due to nonlinearity in strain response because of small displacements of the point of application of the load over the blade surface.

Let us define ε'j as the experimental strain vector (measured on reverse side of the shell and blurred by crosstalk) and εi as the decoupled strain vector. We arrange the relative strains (Bragg shifts) with respect to those of the loaded blade according to a relative strain matrix formalism, as follows:

$$\varepsilon'_j = \frac{K'}{K} \cdot CMj,i \cdot \varepsilon_i\,, \tag{37}$$

where CMj,i is a unitary crosstalk matrix and K'/K is the rigidity ratio due to stress coupling. The factor K'/K is a scalar when the equivalent rigidity K' is the same for all blades, otherwise it is a vector.

The crosstalk compensation procedure proceeds in an iterative way (trial and test). It consists in choosing a ζ-value and calculating the equivalent rigidity K' with the help of Eq. (28)-(31) and (32) for all the connected blades. The coupling parameters $\zeta = 0.44 \pm 0.04$ and $K_f = 636$ N/mm gave the best adjustment with experimental coupling coefficients.

The 2-side theoretical coupling vector (symmetric) is [1, 0.52, 0.27, 0.14, 0.07] and the equivalent rigidities are 886 N/mm and 582 N/mm for 2-side and 1-side cases respectively.

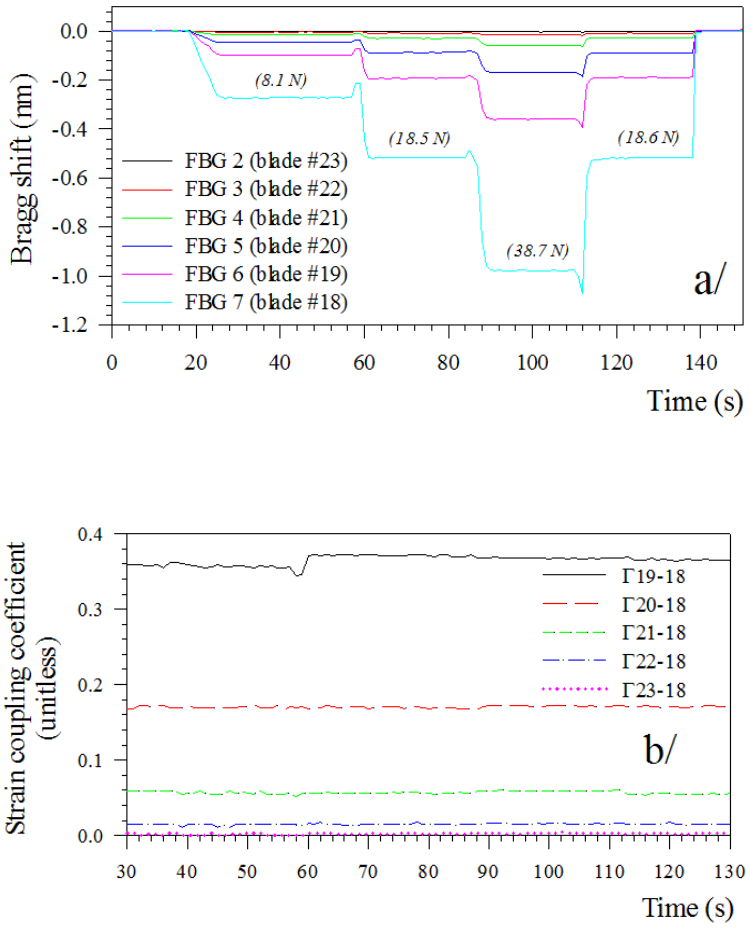

FIG. 18 Evolution of Bragg shifts vs time for several loads applied onto blade #18 (a/) and plot of the coupling coefficients Γi-18 (b/).

For the blade that is free on one side (near the cut) and connected to the other one, the 1-side equations are used, i.e. Eq. (28b)-(31) and (32b). For a blade that is surrounded by connected blades, the 2-side equations are used, i.e. Eq. (28a)-(31) and (32a). For partially-connected blades (i.e. one-blade connected, two blades connected etc.), Eq. (34) was also used.

Then, new sensitivities Σ_f (pm/N) are obtained, corrected for coupling-induced stiffness increase.

As described in III.A.2 and Fig. 6, the Bragg-to-load sensitivity depends on the position of the FBG bonded on reverse side of the blade. As we assume equivalent blades, the experimental dispersion in sensitivity data is solely due to FBG location along the clamp. Therefore, it is necessary to normalize experimental coupling ratios by Bragg-to-load sensitivities before building the experimental crosstalk matrix CM. Practically, this operation proceeds as follows:

$$\Gamma'_{j,i} = \left({}^{\Sigma_{fi}}\!/_{\Sigma_{fj}} \right) \Gamma_{j,i} \,, \tag{38}$$

We then get new crosstalk values that involves only stress coupling effect due to the polymer film. These experimental values (corrected for sensitivity change) are plotted on Fig. 19 along with theoretical crosstalk predicted by the model (IV.C.2) for a film rigidity of K_f = 636 N/mm.

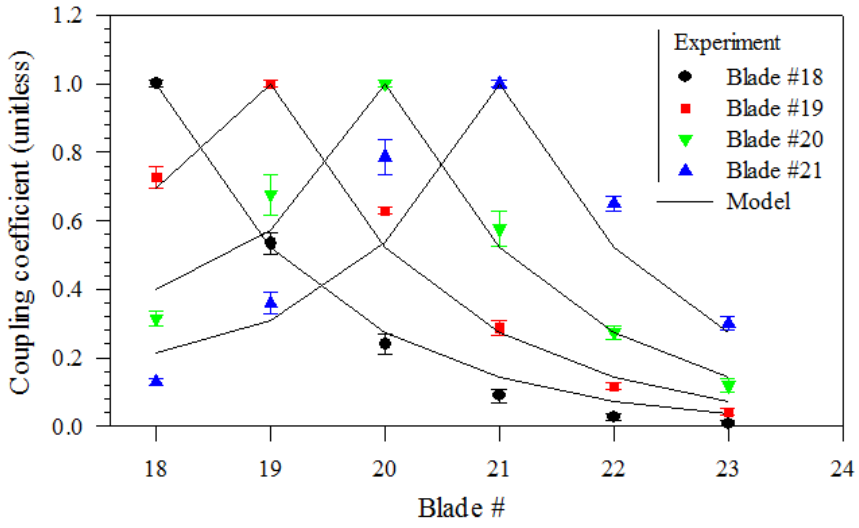

FIG. 19 Plot of coupling coefficients (corrected for sensitivity influence) measured with SL#2 over FBG#1-7 (connected blades #18-24) and adjustment by the analytical model. The ζ-value is 0.44 and the stiffness of each blade is K = 280 N/mm.

Based on the crosstalk model, we build a 7-rank crosstalk unitary matrix composed of the identity matrix and coupling coefficients obtained from Eq. (32).

It is written as follows

$$CMj,i = \begin{bmatrix} 1 & 0.694 & 0.398 & 0.213 & 0.113 & 0.06 & 0.02 \\ 0.521 & 1 & 0.573 & 0.307 & 0.163 & 0.085 & 0.038 \\ 0.272 & 0.521 & 1 & 0.536 & 0.284 & 0.148 & 0.074 \\ 0.142 & 0.272 & 0.521 & 1 & 0.528 & 0.276 & 0.141 \\ 0.074 & 0.142 & 0.272 & 0.521 & 1 & 0.524 & 0.272 \\ 0.038 & 0.074 & 0.142 & 0.272 & 0.521 & 1 & 0.521 \\ 0.02 & 0.038 & 0.074 & 0.141 & 0.272 & 0.521 & 1 \end{bmatrix}, \quad (39)$$

We used it for recovering pressure data from FBG#1-7 (blades #18-24) during the final test on the rolling mill. Each column is an eigenvector (i.e. crosstalk vector along neighboring blades) corresponding to each boundary condition (i.e. 1-side, 1-blade, 2-blade, 3-blade, 2-side). It can be seen that the experimental coupling matrix is not symmetric (i.e. $\Gamma i,j \neq \Gamma j,i$) because coupling coefficients are higher near the cut (1-side model) and lower at the opposite side (2-side model). One may verify that the inverse

matrix applied onto an eigenvector gives back unity for the loaded blade and zero elsewhere (i.e. a concentrated load onto the loaded blade of said eigenvector).

The analytical model fits rather well the experimental data. We attribute the discrepancy to inhomogeneity in epoxy film thickness and to uncertainties associated with renormalization.

Fig. 20 shows the distribution of pressure sensitivity (pm/kPa) along the roll surface and displays the stiffness correction that was applied in accordance with the coupling coefficients shown in Fig. 19. We assume all blades the same and so the same stiffness value (280 N/mm) was used for blades #0-17. The equivalent stiffness increases rapidly for the two closest blades and then reaches a plateau at a value ruled by the 2-side equations.

Finally, Fig. 21 depicts theoretical blade deflections with respect to distance vs blade #0 (stressed blade), determined by the coupling model. We used the same parameters as for Fig. 19 and 20. Fig. 21 also shows the deflections for a silicone film as replacement to epoxy film for water tightness purpose. Weakly cross-linked Polydimethylsiloxane (PDMS) exhibits low Young modulus in the range [0.3 MPa - 1 MPa]. Adjusting the relative amount of curing agent with respect to prepolymer enables to modify PDMS stiffness [21].

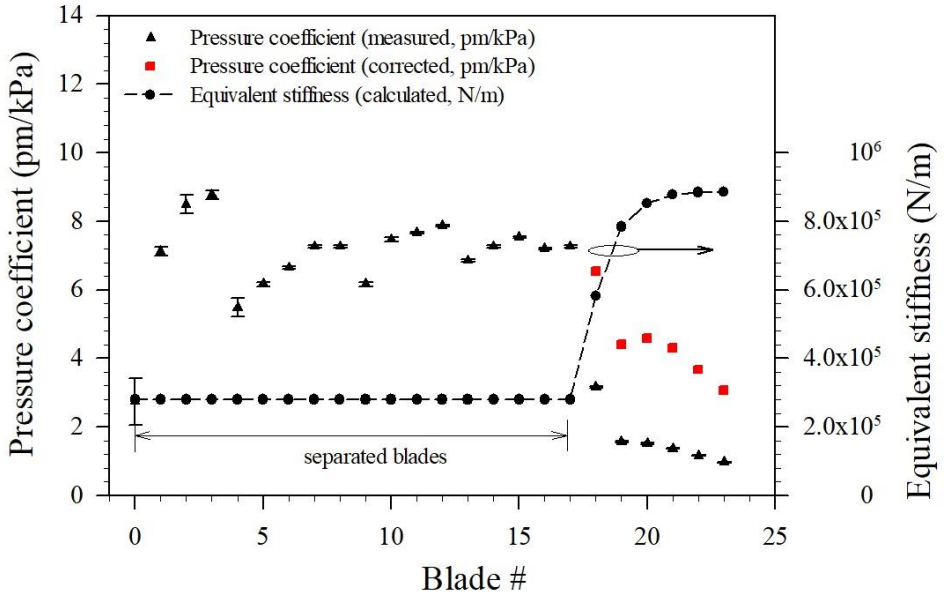

FIG. 20 Distribution of pressure sensitivities (pm/kPa) measured with SL#2 over FBG#2-25 (blades #0-23) (left ordinate) and evolution of the equivalent stiffness K' (right ordinate). The ζ-value is 0.44 and the stiffness of each blade is K = 280 N/mm. Stiffness-correction applied to FBG#2-7 (connected blades #18-23) is also shown.

Let us consider a soft silicone sealant (E_s = 0.3 MPa, Poisson coefficient ~ 0.5). As a preliminary estimation, we consider a thickness of 0.8 mm and 100 % cover of the inner shell surface (bond length = 60 mm).

Fig. 21 shows that only the two nearest silicone-connected blades are actually moved by the loaded blade, opening the way to an efficient matrix inversion of strain data in order to recover contact pressure data distribution on top of roll surface. This inverse calculation relies upon an inverse matrix similar to CMij, but extended up to the entire roll.

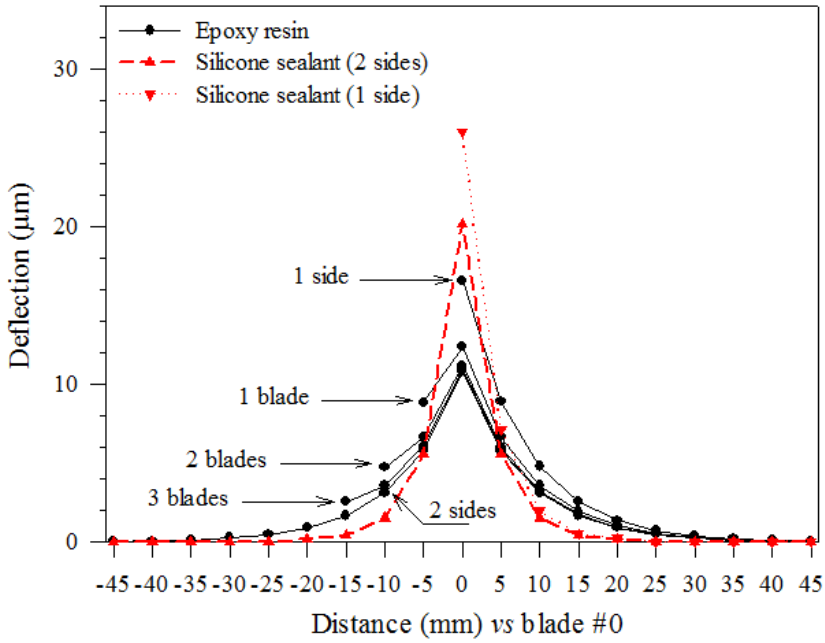

FIG. 21 Plot of blade deflections predicted by the analytical model according to several cases (2 sides, 1 side, 1 blade aside, 2 blades aside, 3 blades aside) and for a force of 10 N applied onto blade #0. Parameters are ζ = 0.44, K = 280 N/mm. Also shown are blade deflections in the case of the appliance of a silicone sealant in replacement to the epoxy film.

2. Pressure sensitivity

For most rolling situations the primary parameter is pressure rather than load, requiring Bragg-to-pressure sensitivities (pm/kPa). However, as far as thin strips are concerned, previous FEM performed by Arcelor-Mittal R&D show that pressure distribution within the contact surface may be considered as nearly uniform along the contact surface (in spite of over-increase in pressure at entrance and exit parts of the contact over the roll surface). In this particular application case, we may consider the resultant force onto each blade as suitable parameter for flatness monitoring, thus simplifying the calibration (only Bragg-to-load sensitivities are necessary).

In the following, we apply Eq. (20b) in order to convert Bragg-to-load sensitivities into Bragg-to-pressure sensitivities, useful for the general case. The reference case is mid-point application for the load as given by Eq. (20a).

The calibration of SL#2 was not performed at mid-point, but one may verify (using moment diagram along blade length) that the change in the point of application of the force this has little influence on the Bragg-to-load sensitivity (a correction factor of 0.9 is used) to account for the change in application-to-clamp distances (13.5 mm). Then, the Bragg-to-load sensitivity is converted into distributed Bragg-to-load sensitivity by using the factor of 3/2 (Cf. III.A.1).

Finally, we calculated the Bragg-to-pressure sensitivity, taking into account the 3/2 ratio. It yields the following transformation:

$$\Sigma_p(pm/kPa) = \left({}^{2s}/_{3}\right) \cdot 0.9 \cdot \Sigma_f(pm/N)\,, \tag{40}$$

where s is the blade surface (s ~ 234 mm^2), from which we get:

$$\Sigma_p(pm/kPa) = 0.137 \cdot \Sigma_f(pm/N)\,, \tag{41}$$

The sensitivity vector Σp (pm/kPa) is plotted in Fig. 22, along with its histogram, again tentatively fitted by a Gaussian distribution. In this case, the Gaussian distribution of the sensitivities of SL#2 exhibits a less goodness-of-fit than with SL#1. The mean value for the sensitivity is -7.2 pm/kPa and the 1-sigma deviation is ± 1 pm/kPa. Compared to SL#1, part of the deviation is likely due to a misalignment of the fiber support with respect to hole axis because the sensitivity tends to decrease gradually along hole axis (as seen on fig. 20).

The Bragg-to-pressure sensitivity of SL#2 is about seven times higher that of SL#1. The increase in sensitivity of SL#2 with respect to SL#1 results from both blade separation and closer clamp bonding. Looking back to FE modeling (Fig. 6), the surface strain is ~-50 ± 10 microstrain for SL#2 and ~-165 ± 10 microstrain for SL#1 which gives an expected strain ratio $\varepsilon(x_2)/\varepsilon(x_1)$ ~ 3.3 ± 0.8. Considering connected blades, the Bragg-to-load sensitivity of SL#1 was 4.4 ± 0.1 pm/N (indentation setup, see IV.B) while that of SL#2 was 12 ± 3pm/N (HBM UR1, see IV.D), i.e. a threefold improvement in sensitivity in accordance with FE modeling. This improvement is mainly due to the smaller clamp-to-FBG distance (both blades are epoxy-connected).

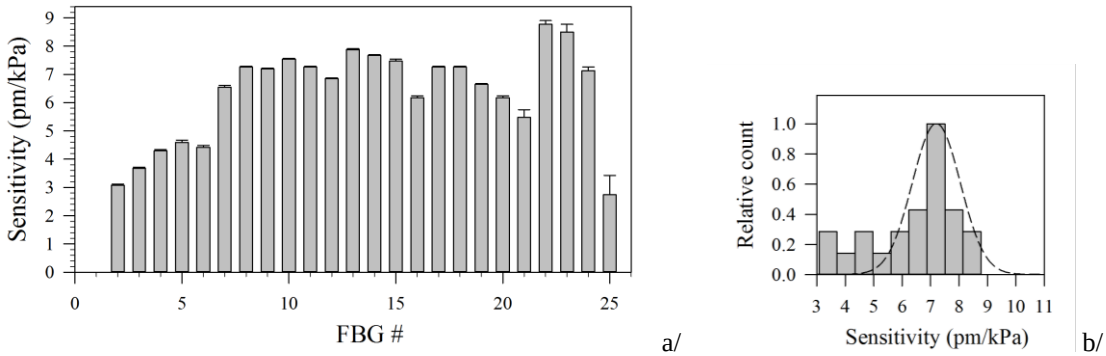

a/ b/

FIG. 22 Calibration chart for SL#2 (in pm/kPa), as obtained from the calibration with a load sensor in AM R&D (a/) along with histogram of sensitivities (b/). FBG#25 is located at the edge of the roll while FBG#1 is located at the middle.

The off-pilot line calibration procedure is simple and cost-optimized. However, it relies on FEM (equivalent 's' surface parameter) in order to transform load data into pressure data, which in the end degrades accuracy. Both calibration procedures lead to consistent average sensitivities of the order of -7.2 pm/kPa for separated blades, in accordance with analytical calculations (see IV.A.2). Taking into account the spectral resolution of FBG units (~ 0.3 pm), it means that the detection limit in contact pressure is about 0.1 kPa, therefore demonstrating the compliance of the roll to rolling specifications.

V. TEST OF THE FBG FLATNESS ROLL PROTOTYPE ON A COLD ROLLING MILL

The objective of this last experiment was to generate flatness defects on aluminum strips and to check the ability of the flatness roll to detect them.

A. Description of the experiment

We tested the prototype roll equipped with SL#2 onto a cold rolling mill available at Constellium C-Tech (Voreppe, France). The rolling mill (Spidem Quarto) needs a minimal strip tension to operate properly. It delivered high contact pressures (several 100 kPa) by simultaneously exerting both pulling force of 300 kgf and hold-on force of 400 kgf, controlled by a Dewetron 400 unit.

The Bragg spectra from FBG#1-7 (blades #18-24) and FBG#8-25 (blades #0-17) were simultaneously monitored by the FBGS and CEA readout units respectively. We used two singlemode 1-channel rotary joints (Princetel MJXA-155) for this purpose. Fig. 23 shows the mounting of flanges and thrust bearings onto both sides of the roll prototype at Constellium premises before being installed next to the rolling mill.

FIG. 23 Mounting of flanges and thrust bearings onto the prototype roll at Constellium premises (Voreppe, France). a/ Flange mounted onto its thrust bearing, b/ and c/ mounting onto the prototype roll.

Constellium engineers installed a dedicated table in order to mount both the uncoiler (providing control of the pulling force) and the flatness roll prototype, as shown in Fig. 24.

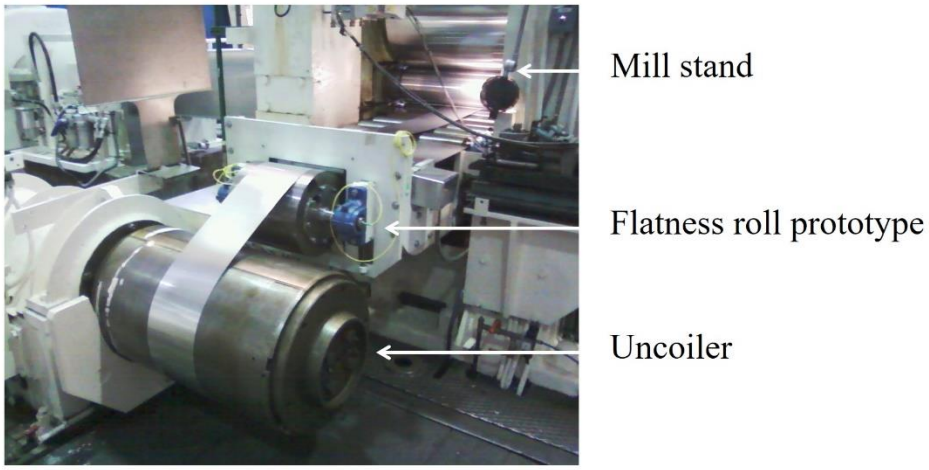

FIG. 24 View of the flatness roll prototype mounted onto the table between the uncoiler and the cage of the Spidem mill stand at Constellium facility.

The rolling parameters for the test are summarized in Table III.

FBGs were mounted on the clamps that enter/leave the contact last (i.e. reverse configuration compared to pilot packaging line). The scan rate of the readout unit of CEA was 960 Hz while the FBGS one was down-tuned at 96 Hz in order to get rid of instabilities in wavelength detection.

Each readout unit operated freely and both signals were post-synchronized. FBG #1 (on roll structure) and #2 (on first blade, near the edge) were set to off because FBG#2 was hardly detected by the readout unit, which generated instability in wavelength detection and storage (the amplitude of the FBG signals was close to detection threshold).

TABLE III. Rolling parameters for the test of the flatness roll prototype.

Rolling parameters	Value	Rem
Metal sheet	Aluminum	
Wrap angle	50°	
Contact length	139 mm	Over blades
Strip thickness	0.3 mm	At exit
Strip width	250 mm	
Linear speed	9 m/min, 18 m/min	
Pulling force	300 kgf	

B. Generation of flatness defects

Constellium engineers intentionally misadjusted the rolling mill to generate huge flatness defects, wavy edges for instance, as shown in Fig. 25.

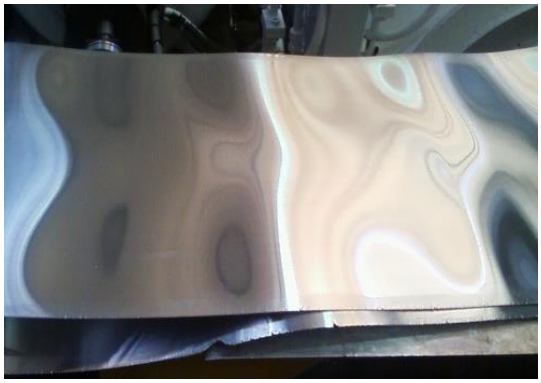

FIG. 25 View of flatness defects (wavy edges) generated by the cold rolling mill.

Several strips passed through the mill and some of them brake by excessive shear stress. The thickness of the aluminum strip was 0.45 mm at the output of the rolling mill. The strip width was 250 mm thus covering the sensing part of roll length. We monitored only half part of it with the prototype roll. Applying Eq. (3), the average contact pressure was 180 kPa.

In Fig. 26, we show two Bragg signals obtained during two successive trials at different linear speeds (i.e. 18 m/min and 9 m/min respectively).

In Fig. 26a, strip break occurred at t ~ 5 seconds. The oscillation of the baseline (off-contact) is due to inertia unbalance of the roll. Compared to previous signals obtained on the packaging pilot line (AM R&D), the data are less stable because of the tampering of the laminating roll. Furthermore, some signals exhibit positive strain (e.g. FBG #4 and #8) despite being covered by the aluminum strip. This abnormal behavior might be due to deleterious friction effect that superimposes over pressure effect. Far enough from the contact entrance (i.e. at the beginning of the strain plateau), friction forces are released and the pressure-induced strain signals appear to be more stable.

This result is in accordance with the previous results obtained on the packaging pilot line (Arcelor-Mittal R&D), irrespective on the FBG orientation inside the shell. No matter on which clamp FBGs are bonded on, because pressure is homogeneous inside the strip-blade contact (particularly for aluminum strip) and the blade length is smaller than contact span in most laminating situations (large wrap angle).

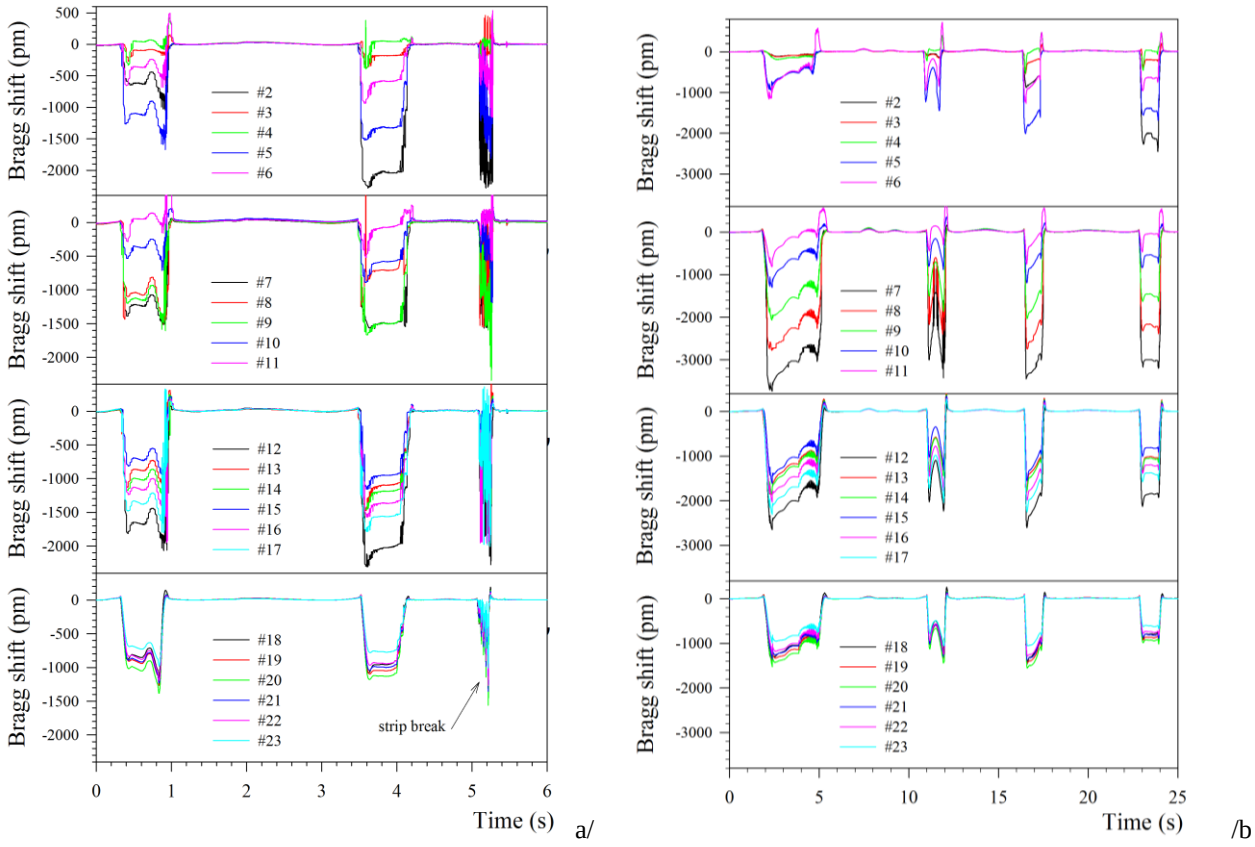

FIG. 26 Example #1 of Bragg shifts obtained with SL#2 during rotation of the prototype roll driven by aluminum strips laminated onto a cold rolling mill (pulling force was 300 kgf). a/ : speed = 18 m/min, b/ speed = 9 m/min.

Bending-induced peaks are less important than with steel strips (Cf. Fig. 11), probably because aluminum is a softer material than steel and because of the smaller wrap angle.

On Fig. 26b, Bragg signals were recorded during the acceleration phase (the time period was not constant). Friction effects might sometimes deform the strain plateau into an inverse V shape. This behavior prompted us to use only the first data points for metrological purpose.

Strain data picked up in the entrance part are used to build the pressure distribution along the roll as it changes during several turns (Fig. 27). To do so, Bragg shifts are converted into pressure changes with the help of the linear relation:

$$P(kPa) = \Delta\lambda(pm)/\Sigma_p(pm/kPa)\ , \qquad (42)$$

where Σ_p is the sensitivity vector calibrated in (IV.D.2).

The inverse calculation was tested on FBG#1-7 (blades #18-24) using the crosstalk matrix (Eq. (39)). The distribution in contact pressure for connected blades was recovered by applying an inverse matrix calculation. A 7-rank matrix was necessary to calculate the 6-component vector because of edge effect that bring large uncertainty for the last blade (to do so, the strain measured on blade #24 was duplicated onto a fictive blade #25 that forces the boundary condition to a physically acceptable value).

Stress crosstalk leads to a strong damping of pressure data which distribution eventually appears flat. Keeping in mind that the roll prototype is only sensitive on its left half-part. The pressure pattern that is shown in Fig. 27b is indeed typical of a wavy edge defect, i.e. pressure increase close to the edge of the strip and minimal in the middle. Pressure oscillations are also visible.

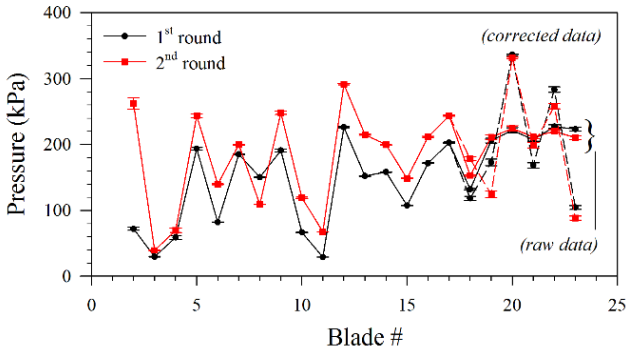

a/

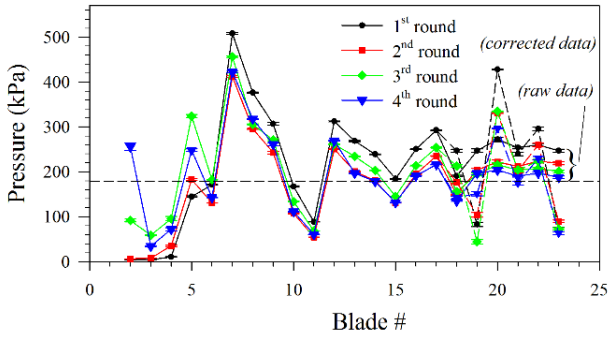

b/

FIG. 27 Pressure distribution calculated from strain signals extracted from Fig. 26a (a/)and 26b (b/) with the help of the calibrated sensitivity vector. Dash-dotted data are decoupled strain using the matrix formalism (IV.D.2).

VI. DISCUSSION AND PERSPECTIVES FOR FUTURE USE

In the following, we get into the details of current limitations and future improvements of the FBG-based roll prototype.

A. Pressure calibration of the roll prototype

Both calibration procedures have advantages and limitations, listed hereafter:

The first method (on-pilot line) consists in recording Bragg data on the packaging pilot line (AM R&D), preferentially at low speed and at the middle part of the roll where strip tension is the most repeatable. In this case, the reference contact pressure (60 kPa) is calculated from strip tension (delivered by the winding machine), strip width and thickness, wrap angle and roll radius. Bragg shifts are then recorded with respect to contact pressure from which pressure sensitivities (pm/kPa) are calculated for each blade.

On pilot line calibration procedure enables to record all sensitivities (pm/kPa) from all blades all in a row, which allows for fast analysis. However, care must be taken to use annealed metal strip, free of internal tension and to operate at low speed and at the middle of the strip that may be moved along the roll surface. A large number of contacts should be recorded in order to improve statistical uncertainty but accuracy in pressure measurement depends on the accuracy of the load monitoring associated with the winding machine.

The second procedure makes use of a point applicator connected in series with a load sensor. Off-pilot line calibration procedure is simple and cost-optimized and as such, is an interesting alternative to the pilot line. Long-term averaging lowers statistical uncertainty. However, this calibration procedure requires to know the ‘s’ parameter (obtained by FEM) with the aim to transform load sensitivity (pm/N) into pressure sensitivity (pm/kPa) which degrades the accuracy figure. As far as the stress vector is concerned, only the deviation with respect to average stress is required. Therefore, off-pilot calibration is an interesting alternative to the pilot line.

Both calibration procedures lead to consistent mean pressure-to-Bragg sensitivities of ~ -7 pm/kPa (free blades), or ~ -55 pm/N once translated into Bragg-to-load sensitivity. They are critically dependent on the FBG-to-clamp distance since high stress gradient occurs in this part of shell. The first sensing line (SL#1) was epoxy-bonded along a first mid-part of the roll at a distance of 12 mm from the clamp. The second sensing line (SL#2) was bonded along the second half-part of the roll, at a FBG-to-clamp distance of 4 mm. The sensitivity of SL#2 in increased by a factor of ~ 3.3 with respect to SL#1 as a result of its location near the clamp.

B. Capability of the flatness roll prototype

We evaluate the metrological performance of the flatness roll prototype by use of the capability C-factor, defined by Eq. (5). From IV.A.2, we got to the conclusion that the detection limit in contact pressure of the prototype roll is about 0.1 kPa for liberated blades (i.e. $\sigma_s \sim 0.1$ kPa). Along with this, Eq. (4) teaches us that the 5-I flatness uncertainty σ_f is 10 kPa for a 0.2-mm thick steel strip. Therefore, Eq. (5) yields a theoretical capability figure of about 9 and 25 for 0.2-mm thick aluminum and steel strips respectively. The C-factors drops down at about 4.5 and 12.5 for 0.1-mm thick strips of same materials, therefore demonstrating that the capability of the FBG-based flatness roll prototype competes with that of commercial rolls.

C. Crosstalk correction

The stress coupling appears to be a major issue with this flatness roll design. A very low indirect crosstalk (less than 0.6 %) is due to reaction from clamps and direct effect of pulling force whereas a high direct crosstalk (40 % to 60 %) is due to epoxy and polymer film support for Bragg gratings before cutting-off.

We propose a model for the stress coupling that fits well experimental data obtained with both SL#1 and SL#2. It predicts the stress coupling induced by any polymer film (e.g. epoxy, silicone). We considered five specific cases corresponding to different boundary conditions (2-side, 1-side, 1-blade aside, 2 blades aside and 3 blades aside).

Furthermore, we invoke the superposition principle in order to generalize the model to a plurality of blades (pressure distribution). We then build an inverse matrix formulation providing the pressure distribution in the contact, from strain data recorded by FBGs on reverse sides of blades. It proved efficient to recover the pressure distribution over uncut blades, despite a strong coupling exerted by the epoxy film. After epoxy cutting, the use of soft silicone is a promising alternative sealant solution to epoxy with low enough crosstalk influence to enable matrix correction.

D. Future improvements

This work provides the proof-of-concept for a FBG-based flatness roll of technological readiness level estimated about 6. Additional work is required before reaching an industrial prototype stage.

1- The metrological performance in cold rolling is to be evaluated with comparative monitoring technologies. As flatness roll, the prototype requires a minimal strip tension (minimal contact pressure) for proper operation that is yet to be determined. The minimal contact pressure has the effect of putting all blades in contact with the strip (thus compensating for machining tolerance of the external surface position).

2- A strong increase in capacity will be necessary in order to cope with the reduction in sensor size. In the current prototype, 25 FBGs are wavelength-multiplexed along a single fiber strand. This demonstration opens the way for a cost-optimized massive instrumentation of meter-long industrial rolls by a thousand FBGs distributed along several sensing lines, parallel to roll axis (typically 4 lines, every 90°).

3- We envision coating a soft silicone sealant on reverse side in order to preserve water tightness. The coupling model teaches us that the impact of a sealant-induced crosstalk is limited to the two closest neighboring blades. The preliminary matrix inversion performed with the epoxy-bonded blades lead us to be confident with our capability to eliminate the crosstalk influence by a silicone sealant.

4- The optical signals were extracted from the roll with the help of singlemode fiber rotary joints. Although this solution enabled us to carry out the demonstration phase, radiofrequency (RF) data link is a more robust solution that seems more appropriate in an industrial context.

5- Self-triggering data acquisition of Bragg wavelengths for both on- and off-contact involves the use of angular encoders.

6- A proof-of-concept was achieved at linear speeds up to 60 m/min. However, linear speed may ultimately reach 4000 m/min on industrial lines. This has two important consequences:

a/ it implies to accurately balance the inertia of the roll,

b/ it requires a high-speed/high-capacity shockproof FBG monitoring device. Although a scan rate of 960 Hz was suitable for demonstration, the required data rate would be of the order of several 10 kHz for industrial rolls, accessible to many commercial readout units.

7- A large dispersion in pressure sensitivity data was noticed. Since the strain sensitivity of FBG is highly reproducible (1.21 pm/µstrain), this dispersion is attributed to the dispersion in FBG positioning along the fiber support. It requires a more careful control of FBG implementation in the future.

VII. CONCLUSIONS

A flatness roll prototype based on a pressure-induced strain sensing concept has been designed, assembled, calibrated and tested on a pilot line by CEA LIST (Saclay, France) and Arcelor-Mittal (Maizières-les-Metz, France). FBG sensors are used as strain gauges because of their multiple advantages (small size, multiplexing capability, etc.). We eventually tested the flatness roll prototype on a rolling mill at Constellium C-TEC premises (Voreppe, France).

The steel-made prototype roll (296 mm in diameter, 300-mm wide) was drilled along its axis by two opposite bores, below the sensing surface. One bore has been machined under the shape of an escutcheon in order to form a shell of constant thickness (1 mm over 44 mm) acting as a pressure sensing membrane of equivalent length 52 mm. It has been saw-cut every 5 mm into parallel blades in order to reduce pressure crosstalk, resulting in fifty 4.5-mm large, 56-mm long parallel shell blades. To our knowledge, this is the smallest ever-achieved spatial resolution for flatness rolls, suitable to thin strip monitoring.

Engineers from Arcelor-Mittal performed FEM of the shell blades with the help of the Creo Parametrics software in order to determine their theoretical pressure-to-strain conversion coefficients. Shells are placed under combined compression and bending and pressure-to-strain sensitivity reaches its maximum near clamps. In this part of shell, the bending moment is dominated by the fixed-end moment. An analytical model for pressure-induced strain is proposed that yields both Bragg-to-load (pm/N) and Bragg-to-pressure sensitivities (pm/kPa) in both concentrated and distributed loading configurations. The analytical model is in accordance with the experimental pressure-induced strain data. Finally, we performed load tests with both load and capacitive sensors that yielded a blade rigidity (280 N/mm) in accordance with the model prediction and show negligible (~ 0.6 %) interblade stress coupling (crosstalk) due to reaction from roll structure. FEM provide deflection-to-load sensitivities in agreement with both analytical model and experiment. On the other hand, the Bragg-to-load sensitivity inferred from FEM is smaller than both experimental and analytical data. Strong stress gradients at the entrance and output strip parts may lead to an underestimation of the contact pressure at mid-part of the strip, over the sensing blades, accounting for the observed discrepancy.

FBGs were bonded on reverse side close to one clamp using a proprietary procedure. The pressure-to-strain sensitivity (pm/kPa) critically depends on the FBG-to-clamp distance since high stress gradient occurs in this part of shell. We performed another saw-cut to remove the strong direct strain coupling that was re-established by the presence of both the glue and polymer film support. As a replacement to the epoxy film, we foresee the use of a soft silicone sealant to preserve watertightness while keeping the crosstalk value at a low value (i.e. restricted to two nearest blades).

As direct and indirect crosstalk seem inevitable in flatness roll technologies, we propose a mathematical model accounting for interblade coupling that gives satisfactory match with experimental data. We build an inverse calculation based on matrix formalism to retrieve the pressure distribution on shell top from strain data recorded on its reverse side, even in presence of a soft silicone sealant.

The resolution in Bragg shift is determined by twice the spectral resolution of the FBG readout unit (~ ± 0.3 pm) at a scan rate of 960 Hz because the Bragg readout is the difference between in- and off-contact Bragg signals. Since the maximum strain allowed in the elastic domain of E335 steel is 1760 µstrain (2130 pm), the relative pressure resolution of the escutcheon-type flatness roll is therefore better than 0.1 % full scale. Temperature compensation is achieved naturally due to roll rotation.

The flatness roll was calibrated with respect to pressure using two methods: on-pilot line and off-pilot line (making use of a load sensor). Both calibration procedures lead to consistent average sensitivities of the order of -7 pm/kPa (for saw-cut, separated blades). The resolution in contact pressure is therefore less than the kPa granted that the uncertainty in Bragg shift detection is about ± 0.6 pm and it the capability is higher than 3 for 0.1-mm thick steel strips.

All these tests provide the proof-of-concept for the FBG-based flatness roll prototype that shows up a unique combination of performances. Several future improvements are foreseen in view of an industrial prototype, such as increase in Bragg readout capacity and scan rate, validation of water tightness using a soft sealant coating, inverse calculation with a coupling matrix formalism, implementation of an RF data link and angular encoder for self-triggering data acquisition and control.

ACKNOWLEDGMENTS

This work was done within the PLATFORM Project (Maîtrise de la planéité des tôles métalliques formées par laminage, ref. ANR-10-RMNP-0019), granted by the French National Research Agency (ANR). We thank Régis Dimitriou (Constellium C-TEC, Voreppe, France) for fruitful discussions about roll technologies and Pascale Pommier, Hugo Coutier, Philippe Garnier, Eric Bovon for the driving of the Spidem rolling mill at C-TEC Constellium. We also wish to thank Sébastien Champenaud, Thomas Lavalard, Nathalie Labbe, Ivan Santi and Wenceslas Guillemin (Arcelor-Mittal Maizières) for their technical participation and for the driving of the pilot lines. Stéphane Rougeault and Julien Lebecq (CEA List) contributed to the preliminary opto-mechanical conception of the device. Pierre Ferdinand (CEA List, now retired) and Hamid Zahrouni (LEM3, CNRS UMR 7239, Université de Lorraine, 57070 Metz, France) contributed to the project management. Many thanks to Georges Christiany (Arcelor Mittal R&D) for his help and photos, and all people involved in the ANR-PLATFORM project for the constructive and pleasant working relationship.

REFERENCES

[1]J. Molleda, R. Usamentiaga and D. F. Garcia, “On-line flatness measurement in the steelmaking industry,” Sensors, vol. 131, pp. 10245-10272, 2013, 10.3390/s130810245.

[2]N. Legrand, K. Swatch, C.C Peirera-Santos, A. Ehrlacher, "Review of shapemeter technologies to measure strip shape in hot and cold rolling conditions," 10th international Rolling Conference, Graz (Austria), 6-9 June 2016.

[3]D-C Wang, H-M. Liu, J. Liu, "Research and development trends of shape control for cold rolling strip," Chin. J. Mech. Eng., Vol. 30, 2017, pp. 1248-1261.

[4]T. Nijhuis, A. Seilinger, T. Kierner, G. Djumlija, "Innovation trends in hot strip rolling," Millenium Steel, 2005, pp. 195-200

[5]R. Kashyap, “Fiber Bragg Gratings,” 2nd Ed., Ac. Press, 2009

[6]A.D. Kersey, M.A. Davis, H.J. Patrick, M. LeBlanc, K.P. Koo, C.G. Atkins, M.A. Putnam, E.J. Friebele, “Fiber Grating Sensors,” J. Lightwave Technol., Vol. 15, N° 8, 1997, pp. 1442-1463

[7]A. Othonos, “Fiber Bragg Gratings,” Rev. Sci. Instrum., Vol. 68, N° 12, 1997, pp. 4309-4341

[8]D.J. Hill, G.A. Cranch, "Gain in hydrostatic pressure sensitivity of coated Fiber Bragg Grating," Electron. Lett., Vol. 35, N° 15, 1999, pp. 1268-1269

[9]W. Ecke, M.W. Schmitt, Y. Shieh, E. Lindner, R. Willsch, “Continuous pressure and temperature monitoring in fast rotating machine rolls using FBG sensor technology,” Optical Fiber Sensor Conference (OFS 22), Beijing (Chian), 15-19 october 2012, Proc. SPIE Vol. 8421, 8421AZ1-4.

[10]A.M. Sen Gupta, "Stresses due to diametral forces on a circular disk with an eccentric hole," J. Appl. Mech., Vol. 22, N° 2, 1955, p. 263-266

[11]K. Miyao, Stresses in a circular disk with an eccentric hole under radial forces," Bull. Japan Society of Mechanical Engineering (JSME), Vol. 1, N° 3, 1958, p. 195-198

[12]S. Timoshenko, "Strength of materials," part I : Elementary theory and problems, Van Nostrand Co., 2nd Ed., 1940

[13]S. Timoshenko, "Strength of materials," part II: Advanced theory and problems, Van Nostrand Co., 2nd Ed., 1940

[14]R.J. Roarks, "Formulas for stress and strain," 4th Ed., McGraw Hill, 1965

[15]S. Timoshenko and S. Woinowsky-Krieger, "Theory of plates and shells," 2nd Ed., McGraw Hill, 1959

[16]T.H.G. Megson, "Structural and stress analysis," 4th Ed., Elsevier, 2019

[17]A.C. Ugural, "Stresses in plates and shells," McGraw-Hill, 1981

[18]F. Ansari, Y. Libo, Mechanics of bond and interface shear transfer in optical fiber sensors, J. Eng. Mech., 124 (4), 1998, pp. 385-394

[19]J. Zhou, Z. Zhou, D. Zhang, Study on strain transfer characteristics of Fiber Bragg Gratings sensors, J. Intel. Mater. Struct., 21, 2010, pp. 1117-1122

[20]R.J.C. Carbas, L.F.M. da Silva, E.A.S. Marques and A.M. Lopes, "Effect of post-cure on the glass transition temperature and mechanical properties of epoxy adhesives," J. Adhes. Sci. Technol., Vol. 27, N° 23, 2013, pp. 2542-2557

[21]G. Belorgey and G. Sauvet, "Organosiloxane block and graft copolymers," Ch.2, in "Silicon-containing polymers: the science and technology of their synthetis," R.G. Jones, W. Ando, J. Chojnowski Ed., Springer, 2000